ARCTIC RESPONSE TECHNOLOGY
OIL SPILL PREPAREDNESS

February 17, 2016

Einar Olason, Sylvain Bouillon and Pierre Rampal

SEA ICE MODEL DEVELOPMENTS

IN VIEW OF OIL SPILL FORECASTING

ARCTIC OIL SPILL RESPONSE TECHNOLOGY – JOINT INDUSTRY PROGRAMME

The oil and gas industry has made significant advances in the ability to detect, contain, and clean up oil spills in arctic environments (Potter et al., 2012). Ongoing research continues to build upon more than fifty years of examining all aspects of oil spill preparedness, oil spill behaviour, and available options for oil spill response in the Arctic marine environment. This research has included hundreds of studies, laboratory and basin experiments and field trials, conducted in the United States, Canada, and Scandinavia. To build on existing research and improve technologies and methodologies for arctic oil spill response, members from the IPIECA-Oil Spill Working Group, Industry Technical Advisory Committee (ITAC) and the American Petroleum Institute-Emergency Preparedness and Response Programme Group formed a joint committee in 2009. The committee's task was to review the oil and gas industry's prior and future work scope on prevention and response to oil spills in ice in order to identify and prioritise technology advances and research needs. One outcome was the recommendation to establish the Arctic Oil Spill Response Technology Joint Industry Programme (JIP) that would undertake targeted research projects identified to improve industry capabilities and coordination in the area of arctic oil spill response.

The JIP was launched in January 2012 and over the course of the programme is carrying out a series of advanced research projects in six key areas: dispersants, environmental effects, trajectory modelling, remote sensing, mechanical recovery, and in situ burning (ISB).

TABLE OF CONTENTS

FIGURES

TABLES

CHAPTER 1. EXECUTIVE SUMMARY

This project involved new model developments and validation techniques to improve sea ice modelling in view of oil spill trajectory forecasting. Three work packages were developed, which are the focus of this report. Work package one, focusing on model development; work package two focusing on evaluation and validation; and work package three, focusing on uncertainties. Data sets of ocean and ice model results for inclusion in oil spill models were produced.

Work package one focused on two new models, the discrete element model (DE) for the marginal ice zone (MIZ) and the elasto-brittle model (EB) for the ice pack. The DE model is a very high-resolution model representing the movement of individual ice floes within the MIZ. It covers a limited area and time span, but delivers unprecedented realism in terms of the simulation of ice floe interactions. The EB model is a continuous model, more similar to classical sea ice models used in both climate and operational model set-ups. The EB model is however radically different from these classical models in many of its aspects. It uses a different rheology than classical models. It is also Lagrangian, meaning that the model grid moves with the ice, preserving much better the dynamical features like cracks, ridges and leads than traditional Eulerian models.

Work package two focused on diffusion and dispersion analysis in the MIZ and the central ice pack. The available buoy observations from the International Arctic Buoy Program (IABP), as well as results from the DE and EB models, and the operational TOPAZ model were used. TOPAZ, like virtually all operational and climate models, uses a traditional Eulerian ocean model coupled to a sea ice model with the common elasto-viscous-plastic (EVP) rheology. The key conclusions of this work package are:

- The EB model simulates the observed mean and fluctuating sea ice drift substantially better than the TOPAZ model.
- The DE model is a promising tool that provides for better understanding the diffusion and dispersion properties of the MIZ.
- From the IABP data set, we quantified the diffusion and dispersion rates in the Arctic pack ice and described how this information is used in oil spill models.

Work package three focused on model uncertainties due to both initial and boundary conditions, as well as the mechanical parameters of the EB model. Here is a list of the main outcomes and conclusions of this work package:

- We produced and validated a lead fraction data set from satellite observations, suitable to initialise the EB model for short-term simulations.
- We tested the sensitivity of the EB model to both initial conditions and the model's mechanical parameters, producing a set of optimal parameters for the model.
- Using this optimal set of parameters we showed that the model reproduces well both the ice drift and the statistical properties of deformation.
- We tested the response of the TOPAZ model to perturbations in the applied atmospheric forcing.
- In the regions close to the ice edge where sea ice is fragmented and moves mainly in free drift mode, the error in the simulated position is mainly due to the uncertainty in the wind forcing and is about 3-5 km (median value) after one day when the drag parameters are well calibrated.

- In the regions where sea ice is thick and compact, the performance of sea ice models is mainly controlled by the rheology, meaning that the benefits of incorporating the EB model into an operational platform could be quite substantial for predicting sea ice motion and the spread of oil spills in such conditions.

CHAPTER 2. INTRODUCTION

For this project NERSC, within an international consortium of partners from highly recognised research institutions in France, Germany, and Norway, proposed completely new sea ice dynamics model developments in view of oil spill forecasting. The project aim was to develop new sea ice modelling approaches, to evaluate both new and existing models, and to analyse the potential errors and uncertainties in the new and existing models. To do this we used the TOPAZ system (run operationally at NERSC) as a reference, and we developed a discrete element model for the marginal ice zone (MIZ) and a continuous model using an elasto-brittle rheology for the pack ice. The work done in this project serves to enhance our understanding of the physics involved in sea ice drift, to improve the models currently used to simulate the sea ice drift, and to deliver high resolution data representing the best available reproduction of sea ice drift and ocean state in the Arctic to be used for oil spill trajectory modelling.

Oil spill trajectory models running at low and mid-latitudes use information about ocean currents, winds and waves to predict where the oil is likely to drift. At high latitudes, and specifically in the Arctic, the presence of sea ice changes drastically how the oil spreads. In the ice, the spread of oil is strongly controlled by the dynamical properties and state of the ice, such as the drift velocity, amount of fractures, concentration, and thickness. Understanding ice dynamics and modelling it properly is therefore a fundamental and key challenge for producing better oil spill predictions in ice-infested waters, both on the short and mid-term.

The sea ice models presently used in the community as input for oil spill modelling in ice-covered waters have limited skills in simulating sea ice dynamics at high spatial and temporal resolutions. In particular, Girard (2009) showed that the widely used viscous-plastic and elastic-viscous-plastic models do not reproduce the observed statistical and scaling properties of Arctic sea ice drift and deformation, properties that are very important for short to mid-term simulation of the sea ice state. Failure to reproduce short and mid-term evolution of the ice by current sea ice models is not surprising, considering that their original scope is climate research. It does, however, strongly indicate the need for improved or new models. Current models are also developed with a focus on the central pack ice, but sea ice motion in the MIZ is very different from the pack ice. There is therefore a need for a different modelling approach for this specific type of ice conditions. These new models for the ice pack and the MIZ need to be based on good understanding of the dynamics as well as rigorous comparison with observations.

This project approaches this challenge of sea ice model development in view of oil spill forecasting in a three-pronged manner, addressing new model development, model evaluation, and uncertainty estimation in separate work packages (figure 1). The model development work package focuses on the development of the new discrete element (DE) model and the elasto-brittle (EB) sea ice model. The model evaluation work package evaluates the new DE and EB models along with the operational TOPAZ model, with a focus on the diffusion and dispersion properties of sea ice. The third work package estimates the error in the TOPAZ system due to errors in the forcing by using ensemble model runs, and the sensitivity of the EB model to initial conditions and mechanical parameters.

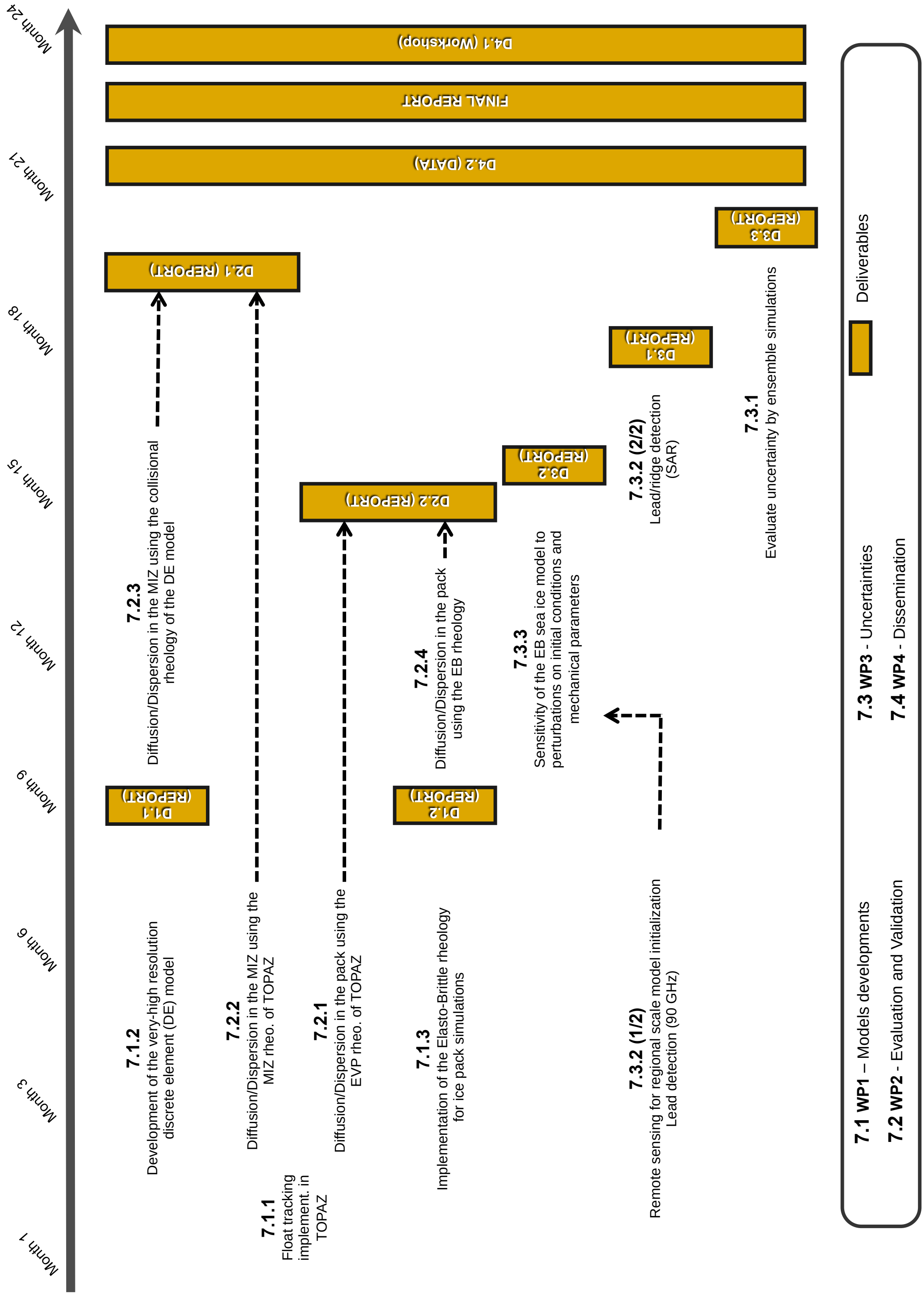

Figure 1: The tasks and deliverables of the project. The figure shows interdependency of tasks as well as approximate schedule for tasks and deliverables

The DE model is a completely new development, even though similar, less sophisticated models have been suggested before. The model's sophisticated and realistic representation of the floe-floe interactions in the MIZ is intended to make up for the lack of observations in the MIZ, allowing us to better understand, simulate, and evaluate the behavior of the ice in such specific ice conditions. The EB model may also be considered new development, even if it is based on the work of Girard2011. In that paper the authors presented a very primitive version of the EB model, demonstrating its considerable potential for the reproduction of the aforementioned statistical and scaling properties. The work done in this project contributes to transforming the EB model from a simple experimental model to a functioning full-scale stand-alone sea ice model.

The second work package concerns model evaluation and focuses on diffusion and dispersion in the DE model, the EB model, and the TOPAZ model. Diffusion analysis provides a clear criterion to separate the mean/predictable motion field from the fluctuating/unpredictable part of the ice motion. It provides reliable information on the mean motion and the diffusivity that can be used to predict the most probable trajectory and the uncertainty around this trajectory. Diffusion is also linked to dispersion, which describes how two particles move apart through time. The two may be used to simulate the spread of an oil spill moving with the ice.

The diffusion/dispersion analysis may be applied at different scales. When applied in the MIZ at the floe scale, it characterises the collisional dynamics, which is analogous to molecular dynamics. When applied in the ice pack at the eddy scales, it reveals the characteristics of the ice mechanical response to the external turbulent forcing (i.e. the wind and ocean surface currents). Knowing the diffusion and dispersion properties of the ice pack, for different conditions and at different scales, is important in an oil spill combat situation when one may need to rapidly estimate the spread of the spill and the size of the search area when only information about the mean ice drift is available. In addition to providing crucial information for oil spill modelling, diffusion and dispersion statistics may also be used to compare modelled and observed sea ice motion and therefore tell us how accurately sea ice models reproduce important characteristics of the drift and how it impacts the quality of the information provided by sea ice forecasting platforms.

The third work package concerns uncertainties in the model results, focusing on the TOPAZ model and the EB model. The TOPAZ system contains a model perturbation system which accounts for the model error by increasing the model spread through perturbation of a number of forcing fields. Running an ensemble of model simulations with different perturbations then allows us to estimate the level of uncertainty in the model results that is due to the error in the forcing fields. Separately the sensitivity of the elasto-brittle model is tested with respect to the model's mechanical parameters and its initial conditions. In order to produce the most reliable initial conditions possible a separate task, dedicated to the remote sensing of the ice conditions is included in the work package.

Each of the three work packages thus aim to improve our ability to model sea ice in view of oil spill forecasting. This is primarily supported by the model development work performed in work package one, while the other work packages consider model evaluation and uncertainty estimates. Through these work packages, the project delivers an assessment of the quality and capabilities of both current, operational models (TOPAZ) and leading research tools (DE and EB models). Combined with a data delivery of model results (deliverable D4.2) the results of the diffusion and dispersion analysis provide important information for simulating oil spill in ice-covered areas with greater accuracy than hitherto possible. The data provided may also be used to test oil spill models in the Arctic in preparation for future oil spill combat situations.

This report consists of three main sections, each outlining the main results of the three work packages and the deliverables of these work packages. Section **Error! Reference source not found.** outlines the results of the first work package, whose subject is model developments. This is followed by a section on the second work package, which focuses on evaluation and validation and section discusses the results of the third work package, dealing with uncertainties. This is then followed by a section outlining the main conclusions of this project.

CHAPTER 3. WP1: DEVELOPMENTS

3.1 D1.1: Development of the very-high resolution discrete element (DE) model

3.1.1 Reminder of tasks

Task 7.1.2 Development of the very-high resolution discrete element (DE) model

Small-scale simulations will be performed over a zone of several km^2, allowing us to resolve the discreteness of the ice cover numerically down to very small scales (hundreds of meters or below). This is in order to perform a fundamental analysis of the spreading of floe trajectories (and consequently of ice-carried pollutants) through time at very small scales, corresponding to the early stages of the oil spill. Simplified but realistic wind forcing fields will be applied in this case, and the initial geometry of the ice field (shapes, sizes and positions of the floes) can be constructed from random distributions of floe sizes using the parameters (maximum and mean floe size) produced by NERSC's wave-in-ice model (WIM).

3.1.2 Introduction

At small scales (100 km) and/or in regions of sea ice concentration smaller than ≈90%, the discontinuous nature of the ice cover must be taken explicitly into account when considering sea ice mechanics and kinematics. This requires a model formulation in terms of an assembly of individual sea ice floes in mechanical interaction. Such a modelling framework is under development at the University J. Fourier/CNRS in Grenoble. It is based on an event-driven algorithm in which particular attention is paid to the collisions between floes. Collisions are simulated such that the floes colliding do not overlap, or penetrate one another, commonly referred to as interpenetration. Between collisions, the motion of individual floes satisfies the linear and angular momentum conservation equations, with classical formulations for the Coriolis effect as well as atmospheric and oceanic skin drags. To deal with collisions before they lead to interpenetration, a linear complementary problem is written with the Signorini-Fishera condition and Coulomb's law for frictional contact. The nature of the contacts is described through a constant coefficient of friction, as well as a coefficient of restitution describing the loss of kinetic energy during the collision resulting from damage and fracturing of the floes in the vicinity of the contact. Each individual floe is meshed with finite-elements, allowing a precise description of any floe geometry and collision scenarios. The floes remain immutable throughout the simulation.

3.1.3 Model description

The model is built as a multi-scale model. At the micro-scale, ice floes are meshed with finite elements in order to describe their geometry, the geometry of the contacts and the integration of external stresses over floe surfaces. At the macro-scale, each ice floe is considered as a discrete object with a unique translational and rotational velocity. The dominating forces acting on the horizontal surfaces of an ice floe result from the atmospheric and oceanic skin drags. Between collisions, the motion of each ice floe satisfies the linear and angular momentum conservation equations.

Unlike most of the models developed previously (Hopkins1996, Hopkins2004b, Herman2011a, Wilchinsky2010), we consider ice floes of any size and shape. To do so, individual ice floes are discretised with finite elements, with realistic configurations retrieved from aerial and satellite images (see figure 2). To discretise each individual floe, we use the finite element method (FEM) associated with the three points Gauss-Legendre quadrature method (Rathod2004). Hence, the external forces are applied on each element mesh and the integration of wind forcing and water drag can be performed over the floe area. Moreover, the ice floe thickness can vary from one element to another over the same floe, although in the present study this possibility was not considered.

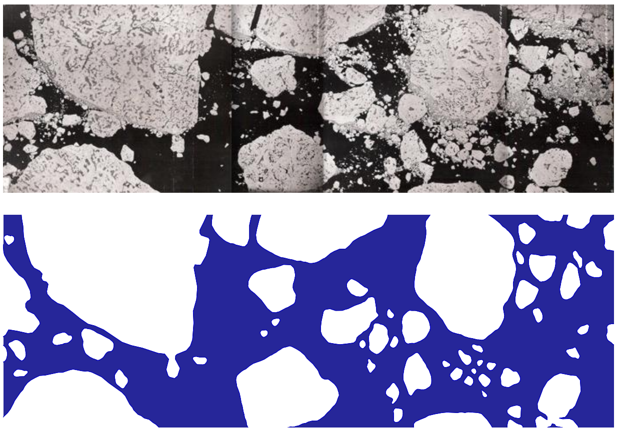

Figure 2: Realistic configuration from an aerial image of the Roberson channel (Northwest Greenland)

To simulate ice floe motion, we use linear and angular momentum conservation and apply an explicit scheme for the temporal discretisation. Generally, implicit integration is preferred to ensure stable behavior for any time step. However, in our model, as we adjust the time step according to ice floe velocities and the distance between ice floes, the explicit integration remains stable. In order to reduce computational cost, ice floes that interact between themselves are grouped into clusters. In a cluster, the ice floes evolve with the same time step and each cluster evolves at its own pace. When several clusters interact with each other, a suitable time step is found to avoid interpenetration and the clusters are gathered together in a single cluster.

Knowing ice floe velocities and positions, an estimation for future motion is performed. This allows the model to predict the potential contact points and the time step is adjusted to avoid interpenetration. Having built a contact frames associated with each contact point we deal with the resulting collisions. This consists of writing a linear complementarity problem (Cottle1992) with constraints from the collision geometrical data. The constraints are a non-interpenetration constraint and a friction constraint based on Coulombic friction. A restitution coefficient describes the loss of kinetic energy during the collision resulting from damage and fracturing of the floes in the vicinity of the contact. In this framework, the normal and tangential impulses are the unknowns.

The definition of clusters should be handled with care, as it may lead to interpenetration or missing collisions. In order to avoid this, we start by adapting the bounding volume hierarchy (BHV) algorithms (Hamlin1992, Quinlan1994) to our framework, with disks to approximate the ice floe shapes. Additionally, our model is based on an event-driven algorithm (McNamara2011), to handle collisions. In figure 3, we present a configuration with its cluster structure, where the ice floes with the same colour belong to the same cluster.

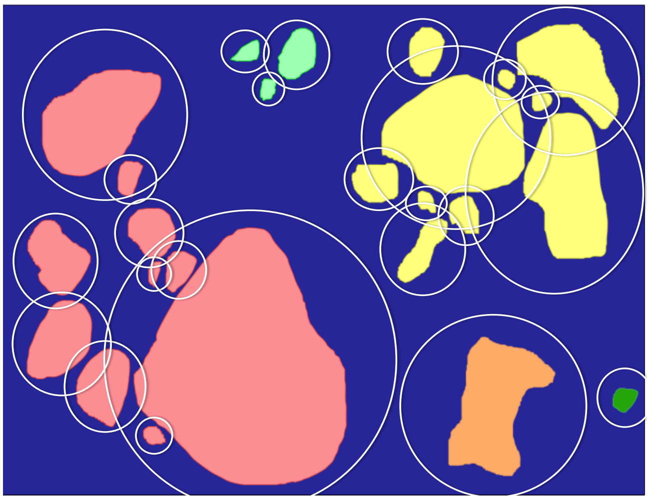

Figure 3: Ice floes grouped into cluster

3.1.4 Model validation

To validate our model and particularly the collision algorithm, a two-step strategy was used. First, we tested our model with typical collision scenarios, i.e. Bernoulli's problem, Newton's cradle, and the sliding box. In addition, we also considered a simplified theoretical collision case. This allows us to check that our model respects different classical conditions for collisions, such as whether symmetry is preserved, whether kinetic energy does not increase, whether ice floes that were previously in contact break away from each other as a result of impact, and whether friction satisfies Coulomb's model. We also tested our model against measurements performed in a test basin, where ice floes were replaced by pieces of wood with a circular shape.

To test symmetry conservation, we tested our model on Bernoulli's problem. This problem consists of simulating the collision between three spheres on the plane where two of them are initially at rest and the third has an initial velocity along the symmetry line directed toward the other two (see figure 4). Our test shows that the model preserves the symmetry of the initial set-up.

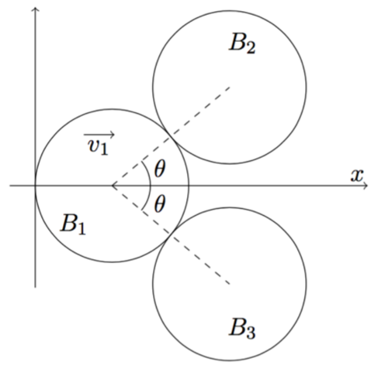

Figure 4: Bernoulli's problem

We test shock propagation through Newton's cradle problem. This is one of the most basic multi-impacts problem one may consider. It consists of simulating the collision between three identical aligned spheres, two of which are initially at rest and the remaining one has an initial velocity along the alignment (see figure 5). There exists an infinite number of solutions, depending on the energy dispersion. Our model allows us to cover a sub-set of the set of solutions by varying the restitution coefficient.

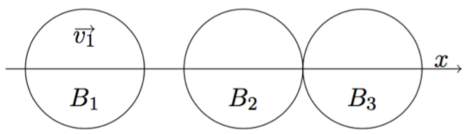

Figure 5: Newton's cradle

Frictional collision was tested using a sliding box scenario. This collision scenario consists of simulating the motion of a box, initially at rest, pushed on a plane. We use a similar configuration as the one of Drumwright (2011). The results obtained for different friction coefficients show that our model is consistent with Coulomb's model.

We validated our model against collision experiments performed in a test basin. These experiments consisted of collisions between two identical disks of wood of the same weight, in the absence of wind and current. They consisted of pushing one disk towards another disk initially floating at rest and repeating this a number of times in order to explore different conditions. Nine collisions were performed and recorded with a camera. Image processing was performed to extract the positions and velocities of the centers of mass of the two disks as a function of time (Dumont2013). The restitution coefficient was adjusted to minimise the gap between the simulated and extracted trajectories, resulting in very good agreement between model and experiments (see report D1.1, section 5.2).

3.1.5 Conclusions

We have developed a new discrete element model of sea ice, specifically to model ice behavior in the marginal ice zone (MIZ). Our model allows us to consider ice floes of any size and shape, with realistic configurations and information on floe size distributions from areal and satellite images. The collision of floes is handled without interpenetration, with the friction between floes based on Coulombic friction and a restitution coefficient to describe the loss of kinetic energy during the collision. We also tested the model against both classical collision set-ups and laboratory tests. Our tests show that the model is well in line with both theoretical expectations and the results of the laboratory tests.

3.2 D1.2: Implementation of the elasto-brittle rheology for the ice pack simulations

3.2.1 Reminder of tasks

Task 7.1.3 Implementation of the elasto-brittle rheology for the ice pack simulations

This task will incorporate the developments of the ongoing Kara Sea modelling project funded by TOTAL E&P. We will set up and perform sea ice (only) simulations using atmospheric forcing from ERA-interim and oceanic forcing from our HYCOM model. Initial conditions will be provided by remote sensing images (see section 7.3.2 of the proposal). In a first phase, we will test the elasto-brittle model (EB) under quasi-static ice approximation by using the finite-element model developed and presented in Girard2011. Then we will proceed with the second phase that will consist on implementing the elasto-brittle rheology within an adequate framework that can be used for simulations of up to 2-3 weeks (relevant duration for dispersion analyses). For the first time, we will produce sea ice forecasts (motion, ridges and leads) computed in a different mechanical framework than the classical and most largely used plastic framework (VP and EVP rheologies).

3.2.2 Introduction

The sea ice models presently used in the community as input for oil spill modelling in ice-covered waters have limited skills in simulating accurate sea ice drift at high resolution since their original scope is climate research rather than operational forecasts. The reason for their inaccuracy may be that they poorly resolve the deformation fields at small spatial and temporal scales (Kwok2008) and fail to reproduce the observed statistical properties of sea ice drift and deformation (Girard2009). The sea ice rheological model is a good candidate to attribute these shortcomings to, since it specifically controls the way sea ice moves and deforms under external stresses. Most of the current sea ice models are based on the same isotropic plastic rheology (Coon2007) and differ only by the choice of different numerical schemes to solve the momentum equation (e.g., VP (Hibler1977), EVP (Hunke1997), JFNK (Lemieux2010)) or by using slightly different constitutive laws, yield curves and parameters. One can then argue that a new and more realistic approach should be proposed to simulate ice dynamics in general, and ice drift in particular, in the context of oil spill trajectory modelling in ice-infested waters.

This task presents a new sea ice dynamical model that aims at better simulating sea ice displacements and deformation at high temporal and spatial resolutions, especially in the pack ice.

ariance properties
ce is a frequent
le is redistributed
f turbulence down
ainly coming from
$_d \approx$ 3–6 days and
the ocean but a

ese events last a
2004a). At scales
g properties over
reds of meters to
iversal in complex
er of components
y models built as
ls) are capable of
nodel we propose
itrano1999). This
and the complex

e consider the ice
ach element may
merges from their
sh having a mean
stress tensor are
le vertices.

nilar to those used
ally integrated sea
ge is controlled by

ess $\dot{\sigma}$ is related to

(1)

Here Y is the sea ice elastic modulus and d is the damage variable equal to zero for undamaged ice and 1 for completely damaged ice. $f(A)$ is a function parametrizing the effect of compactness and is equal to 1 when the concentration A is equal to 1 and strongly decreases with A.

Sea ice is damaged (i.e. d increases) when the internal stress is outside a failure envelope. According to in-situ stress measurements, the failure envelope is well represented by a combination of a Mohr-Coulomb criterion, a tensile stress criterion and a compressive stress criterion (RichterMenge2002, Weiss2007).

A healing process (i.e. d decreases) is parametrised as a relaxation of sea ice damage towards 0. For the simulations presented in this part of the report, the healing is deactivated by setting the damage relaxation time to a very large value. This is suitable for model runs shorter than about a month.

3.2.5 Implementation

The element-based approach allows the presence of discontinuities in the simulated fields at the scale of the elements (e.g. highly localised deformation). This constrains many aspects of the implementation of the model in terms of temporal and spatial discretisation, advection scheme and adaptation of the mesh.

The temporal discretisation defines how the variables evolve from time step n to time step n+1. In the EB model the momentum and internal stress evolution equations are solved together with an implicit scheme to avoid the stability constraint due to elastic waves. Note that the symmetric part of the ocean drag term is treated implicitly, whereas the anti-symmetric part is treated explicitly to preserve the symmetry of the system that needs to be solved. The other evolution equations are decoupled and trivial to solve.

The spatial discretisation of the momentum equation is made with the finite element method. The finite element method consists of approximating the solution as a linear combinations of shape functions, that are in our case piecewise linear. The obtained linear system is then solved with the CHOLMOD implicit linear solver (Chen2008), which is based on supernodal sparse Cholesky factorisation. The other equations are defined locally for each triangle, meaning that no discretisation method is needed.

The advection scheme is based on a purely Lagrangian approach to preserve the discontinuities at the scale of the elements and to avoid numerical diffusion associated with classical Eulerian schemes. The vertices of the element (i.e. the nodes of the grid) move with the sea ice velocity u. The material derivative is then simply equal to the temporal derivative $\frac{\partial \phi}{\partial t}$ relative to the moving mesh so that the quantities are naturally transported with the ice.

We have also implemented an adaptive remeshing scheme using the BAMG mesher (Hecht1998) as implemented in the Ice Sheet System Model (Larour2012). The BAMG mesher attempts to conserve the nodes present in the original grid, but generates new nodes and elements when the elements are too deformed. The criteria for remeshing may depend on the smallest angle between two sides of an element, the length of the element sides, or the area of the element.

3.2.6 Set-up

The first step to set-up the model is to generate the initial triangular mesh for the model domain. The Lagrangian approach imposes us to use unstructured meshes. We choose to use triangular meshes for their flexibility and the existence of efficient remeshing algorithms.

The forcing fields consist of the 3-hourly 10-meter wind velocities from the ASR reanalysis, distributed at 30 km spatial resolution (ByrdPolarResearchCenter2012), and the daily sea surface height and ocean velocities at 30-meter from the TOPAZ system, at an average spatial resolution of 12.5 km in the Arctic (Sakov2012).

For sea ice concentration two different initial conditions are used: either the sea ice concentration from the TOPAZ reanalysis, or a combination of the sea ice concentration and lead area fraction coming respectively from two different datasets derived from the AMSR-E satellite observations.

3.2.7 Preliminary results

The analysis of the simulated sea ice dynamics is performed for the last 3 days of the 10-day simulations. The sea ice velocity field, defined at 3-days' time scale, exhibits realistic spatial discontinuities (see figure 6). The discontinuities in the sea ice motion field cause sharp transitions in the shear and divergence rates, which appear like linear features spanning the entire Arctic basin and look very similar to observed linear kinematics features (see figure 7).

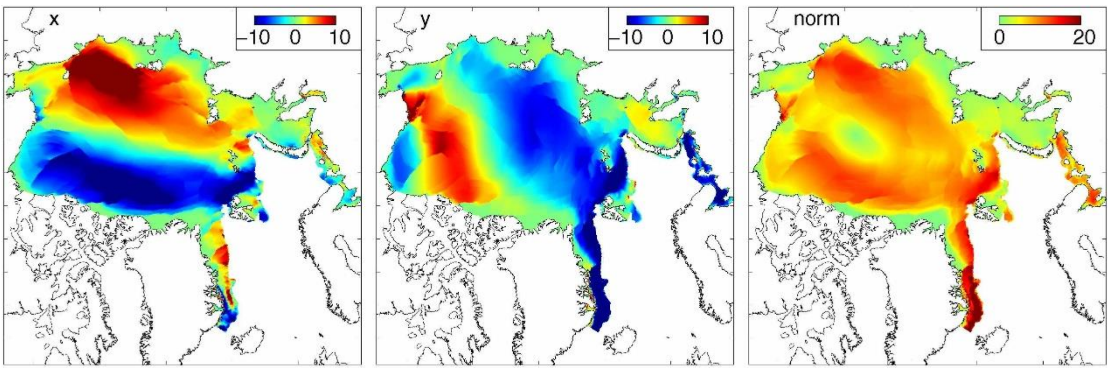

Figure 6: x-component and y-component of the sea ice velocity, as well as its speed (in km/day) computed over the last 3 days of the reference simulation (from 12 to 15 March 2008).

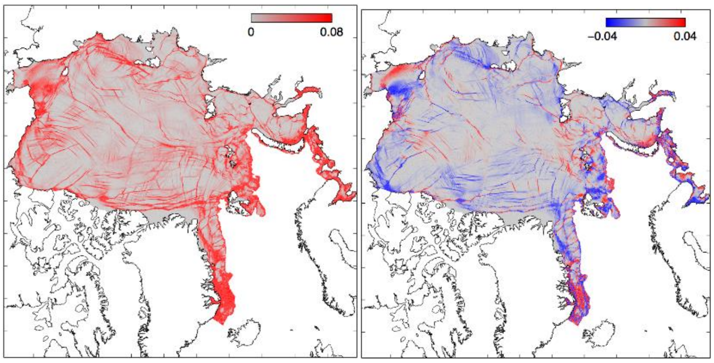

Figure 7: Sea ice shear rate (left) and divergence (right) rates (in 1/day) computed over the last 3 days of the reference simulation (from 12 to 15 March 2008).

3.2.8 Conclusions

The EB model produces realistic motion and deformation fields, exhibiting discontinuities and strong spatial localisation of the deformation, as seen in reality (report D1.2, section 8). Two sets of initial conditions for sea ice concentration and thickness are used, one is only based on the TOPAZ reanalysis while the other one also takes into account estimates of the sea ice concentration and lead area fraction derived from the AMSR-E satellite.

CHAPTER 4. WP2: EVALUATION AND VALIDATION

4.1 D2.1: Diffusion and dispersion laws in the MIZ

4.1.1 Reminder of tasks

Task 7.2.2 Diffusion/Dispersion in the MIZ using the MIZ rheology

We will run simulations for the Barents Sea and track thousands of floats in an area with typical MIZ sea ice conditions and we will perform the same analyses as in the Task 7.2.1.

Task 7.2.3 Diffusion/Dispersion in the MIZ using the collisional rheology of the DE model

The task 7.1.2 will provide ice motion vectors for each floe in the simulation. In a similar way that has been done in regional finite difference models (Task 7.2.2), the trajectories of a large number of ice floes will therefore be followed and analysed to derive dispersion characteristics. We will compare these characteristics with those produced by the MIZ rheology.

4.1.2 Introduction

The main objective of this deliverable is to study sea ice dynamical behavior in the marginal ice zone (MIZ) to provide relevant information for oil spill models. The MIZ is a transition zone between the ice pack and the open ocean, where the sea ice cover is highly fragmented due to the action of waves. The width of the MIZ may vary from a hundred meters to hundreds of kilometers. The MIZ is also characterised by its specific dynamical regime dominated by collisions between ice floes. These characteristics have to be taken into account when modelling oil spills in these conditions.

The discrete element model (DE) gives us a unique opportunity to study processes in the MIZ because it contains sophisticated physics to resolve the collisions between individual ice floes. The TOPAZ model is also unique amongst other Eulerian sea ice models as it includes a so-called “MIZ sea ice rheology”, which is based on a sub-grid scale parametrisation of the floe collisions.

The original idea was to apply the same diffusion and dispersion analysis to the output of the DE and MIZ models for similar conditions, and to compare the obtained characteristics. However, it appears that such comparison may not be relevant because the diffusion regimes simulated by the DE model and the MIZ model are not the same. On one hand, the DE model explicitly simulates diffusion and dispersion due to erratic collisions between floes, but cannot provide information on the diffusion and dispersion due to passing eddies and atmospheric perturbations because it cannot run on large enough areas and on long enough periods. It would require substantial work in optimizing and parallelizing the model for it to run on large enough areas and for long enough periods. On the other hand, the MIZ model can run on long periods and large domains, but it does not explicitly simulate collisions between floes.

In this report, we present the results of the diffusion/dispersion analysis applied to the DE model. The outcome of this analysis is compared to theoretical considerations and to observations. In the discussion, we discuss how the MIZ rheology could benefit from this new knowledge.

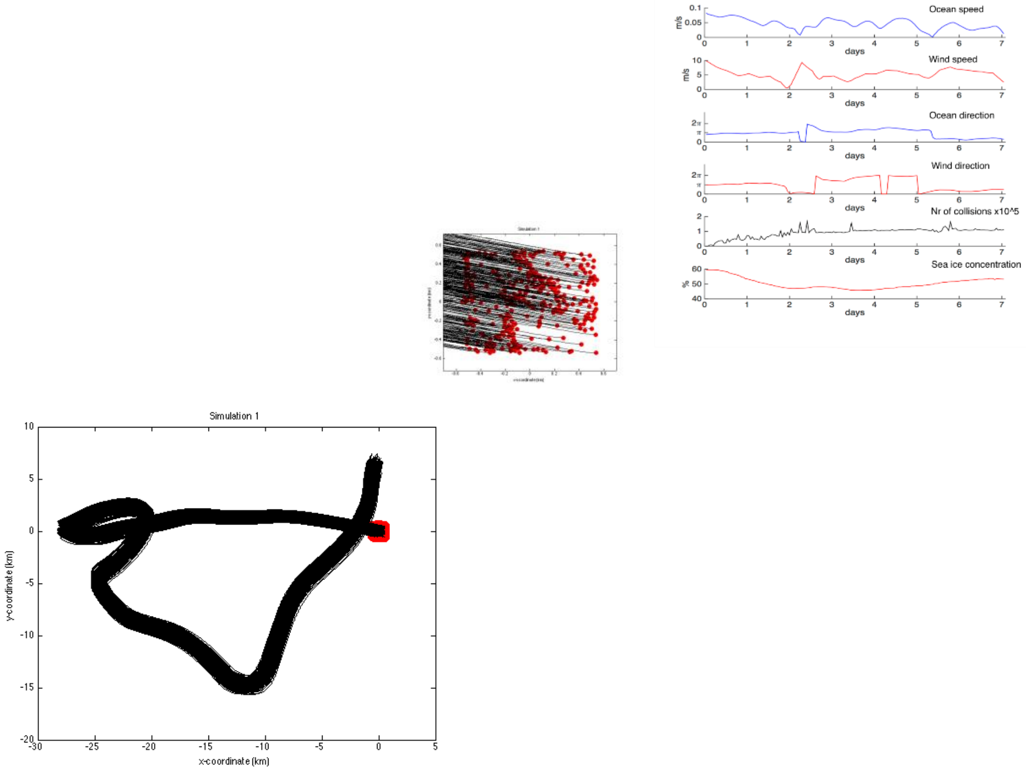

Figure 8: Discrete Element Model Simulation 1 with variable wind forcing and free boundary conditions, a) tracks of the floes with the initial central floe positions indicated by red circles, and overlaid to the lower right is a zoom in of the initial positions, b) the applied atmospheric and oceanic forcing, taken from the TOPAZ model, together with modelled sea ice concentration and number of floe collisions.

4.1.3 Data

The discrete-element model is set up for an initial 1.2×1.2 km domain with 350 floes of variable size and shape. The floe size distribution follows a power law with an exponent of 1.35 and a maximum floe size of 245 m, as observed on satellite images. The shapes of the floes are taken from a catalogue made of floe shapes retrieved from sea ice photos. Several experiments are conducted with different sea ice concentrations varying from 60% to 70%. Two different lateral boundary conditions are applied, i) free boundary conditions (also called open boundary condition **OB**) allowing floes to freely move across the boundaries of the model domain with no resistance and ii) periodic boundary conditions (**PB**) where floe shapes and motions are mirrored from the opposite-side boundary. Uniform forcing is applied over the model domain with wind speed and ocean currents time series extracted at a TOPAZ grid point located at the center of the domain over which the TOPAZ MIZ experiments are performed (see figure 8). We analyse here four experiments, each corresponding to 7-days simulations for which the floe positions were output every 600 s.

4.1.4 Methods

To focus on the fluctuating velocities related to the collisions, we first need to subtract a mean velocity field defined by averaging the motion field at the spatial and temporal scales, *L* and *T*. To study how the applied averaging scales influence the extracted mean velocity field we calculate a power spectral density (PSD) estimate of the energy content in the mean field ū, the fluctuating field *u*' and the total velocity field *u*. The comparison of these estimates indicates which part of the energy spectrum of the total velocity field is included in the remaining (fluctuating) part. Only the fluctuating velocities are used for the diffusion analysis and the computation of the diffusivity *K*. The spectral estimate is calculated with a Welch average method using a Hamming window with 50% overlap. We used floe trajectories of 7 days.

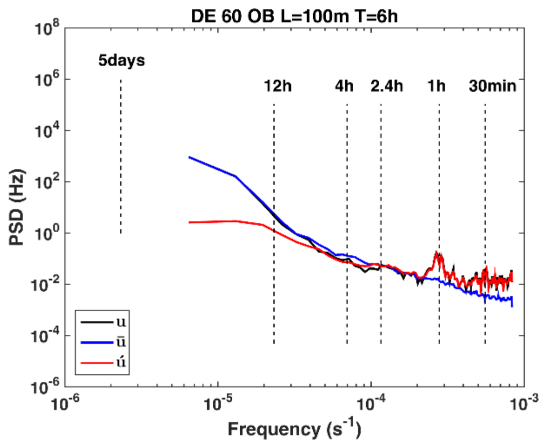

Figure 9: Power spectral density of the original (u), the mean (ū), and the fluctuating (u') velocity components for the averaging scale L=100 m and T=6 h for simulation DE 60 OB with 60% sea ice concentration and open boundary. Some selected general key periods are indicated with black vertical dotted lines.

Figure 9 shows how the energy in the original velocity fields (black lines) may be compared to the energy in the mean ū (blue lines) and fluctuating *u*' (red lines) velocity fields. We note that for *L*=100 m and *T*=6 h the low frequency energy is extracted into the mean velocity field (the blue lines) while the high frequency energy is included in the fluctuating velocity field (the red lines), with peaks in the energy around 1 h and 30 min. We concluded that these averaging scales are well suited to define the “collisional” domain.

4.1.5 Results

Another way to see that the averaging scales *L*=100 m and *T*=6 h are well chosen is to look at the integral time scale (see definition in report D2.1). In all simulations, a clear plateau of nearly constant integral time scale of around 2 h exists for averaging scales larger than 6 h and 100 m (figure 10). The averaging scales *L*=100 m and *T*=6 h are then used to compute the integral time scales Γ and the diffusion coefficients K. Those are found to be similar in all the simulations with values Γ~2 h and K~1.0 m^2s^{-1}.

Observations of ice floes dynamics in the MIZ are scarce but some do exist. There is for example the MIZEX expedition, whose data was used by Shen (1986), Shen (1987) to develop the MIZ rheology. Here we compared the standard deviation of the fluctuating velocity simulated by the DE model to the one observed during this expedition and found the same order of magnitude. The variance from the model is between 1.3–1.4 cm^2/s^2 (with concentration of nearly 60 and 70%, L=100 m and T=6 h), corresponding to a standard deviation of 1.15 cm/s, whereas the standard deviation from the MIZEX experiment is 0.46 cm/s (with concentration of nearly 80%, L=5 km and T=8 h). In their study Shen (1986), Shen (1987) also discuss the theoretical value predicted by the MIZ rheology and found it was one order of magnitude lower than the value computed from observations. They pointed to four factors that could contribute to this discrepancy: floe diameter, floe irregularities, material properties, and other sources of fluctuations (e.g., external forces). These factors are potentially crucial for reproducing MIZ dynamics and are better addressed now with the DE model. However, a detailed comparison of the DE model against observations using consistent averaging scales would be needed to conclude.

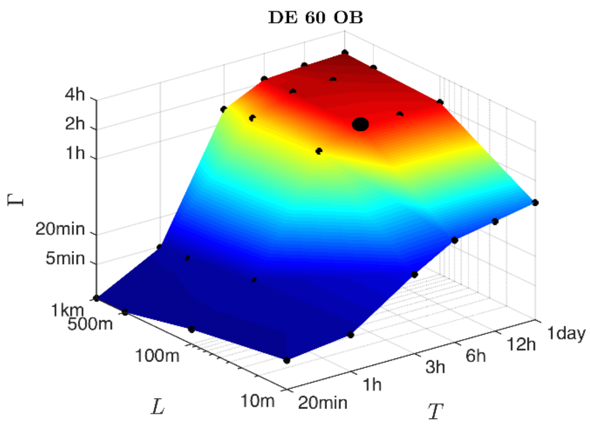

Figure 10: Integral time scale **Γ** for DE 60 OB for different spatial, L, and temporal, T, averaging scales. The selected averaging scales for the “collisional” domain, L=100 m and T=6 h, are shown with a larger black dot.

The distribution of the fluctuating speed (absolute velocity) is presented in figure 1. The fluctuating speed follows an exponential distribution for the major part of the distribution (i.e. up to 4 cm/s), but deviates slightly from the exponential fit for the higher velocities. We do not have data in the MIZ to validate this distribution, but we know that for the ice pack exponential distributions are expected and observed.

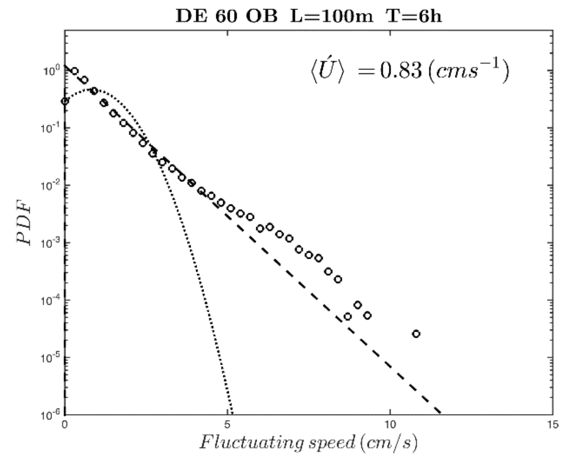

Figure 11: Probability density function for the fluctuating speed U' for DE 60 OB with L=100 m and T=6 h. The lines of the normal distribution fit (grey line) and the exponential distribution fit (black dotted) are indicated.

Using the calculated fluctuating velocity components, *u*' and *v*', we calculate the fluctuating displacement, r_x and r_y. Figure 12 shows the variance $<r'^2>$ of the fluctuating displacements for simulations at two different concentration values. All the simulations seem to capture the t^2 growth in the initial ballistic regime. However, the rate of change for longer time periods $t>\Gamma$ does not follow the theoretical t^1 growth rate. This could indicate that eddies and atmospheric perturbations are still active at this scale (*L*=100 m and *T*=6 h) and thus impact the statistics. For purely molecular diffusion, the variance $<r'^2>$ should always increase as t^1.

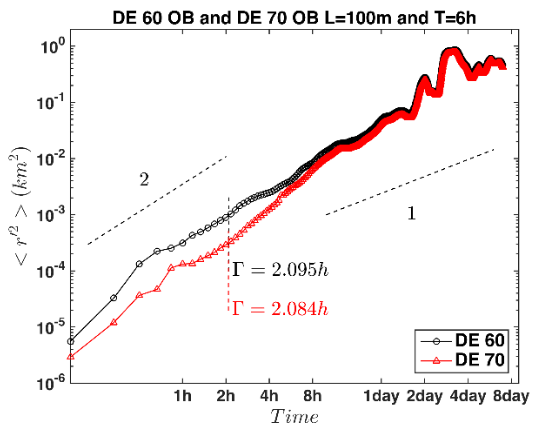

Figure 12: Variance of the fluctuating displacement <r'2> for DE 60 OB (black) is compared to DE 70 OB (red) with averaging scales L=100 m and T=6 h. The calculated integral time scale **Γ** as well as the growth rate slopes of t1 and t2 are indicated (dashed lines).

For several pairs of ice floes in the DE model, we study how the separation *L* changes during the time from the initial separation, *L*(0), to the separation after a time τ, *L*(τ), and calculate the change in the separation over time as $\Delta r = \|L(\tau) - L(0)\|$. This indicates how much an area of initial size *L*(0), for instance an area of sea ice mixed with oil. will disperse over a time τ. In a purely collisional regime, the absolute value of dispersion, $<\Delta r^2>$, increases with time τ but should not depend on the initial separation distance $L(0)$. We divide the analysis into three bins according to the initial separations considered: L50m (10 m $<L(0)<$100 m), L300m (100 m $<L(0)<$500 m), and L800m (500 m $<L(0)<$1200 m). We calculate the dispersion for time intervals ranging from τ=10 min to τ=4 days. With a minimum of 2702 floe pairs in each $L(0)$–τ category, all calculations presented here are statistically robust.

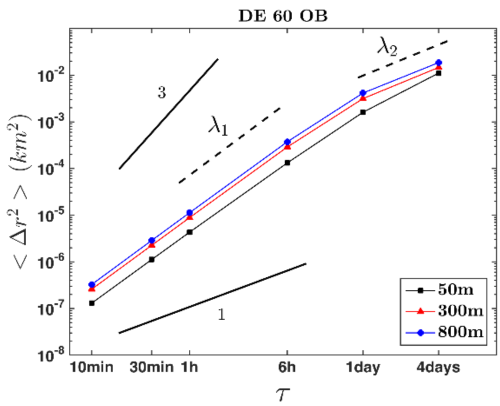

Figure 13: Dispersion in the Discrete Element Model DE 60 OB with 60% sea ice maximum sea ice concentration and open boundary condition, described by the mean square change in separation, $\langle \Delta \boldsymbol{r}^2 \rangle$, as a function of time $\boldsymbol{\tau}$. Lines of power law approximation are indicated for $\boldsymbol{\tau}$<1 day ($\boldsymbol{\lambda}_1$) and for $\boldsymbol{\tau}$>1 day ($\boldsymbol{\lambda}_2$).

As shown in figure 13 the dispersion rate may be represented by a power law scaling, $\langle \Delta r^2 \rangle \sim \tau^{\lambda}$ where λ describes the growth rate of dispersion. λ values are calculated for two-dispersion time intervals τ<1 day and τ>1 day. The results for τ>1 day are only based on two points and therefore only give an indication of a change in dispersion regime, but may not be quantitatively correct. λ_1 values for τ<1 day are very close to 2 (about 1.9) in all simulations, which corresponds to the theoretical exponent for turbulent diffusion (Batchelor1952) and observed exponent (Martin1985) for small τ. The results for τ>1 day show that λ~1.1, which is very close to theoretical and observed exponents for the ballistic regime (Batchelor1952, Martin1985).

We estimate the power law scaling of the dispersion as a function of the initial separation between ice floes $\langle \Delta r^2 \rangle \sim L(0)^{\beta}$. All DE model results are relatively low, in the range 0.17<β<0.48, indicating close to homogeneous deformation. The slope β is lower with periodic boundary conditions and increase with increased sea ice concentration as the system is becoming closer to pack ice conditions. For comparison, this exponent is generally close to zero, for dispersion only due to molecular diffusion, close to 1 for dispersion at the ocean surface and close to 1.8 for dispersion in the ice pack (Martin1985).

4.1.6 Discussion

For the DE model on one hand and for the TOPAZ model on the other the temporal and spatial resolution as well as the size of the domains are very different. Considerable efforts in optimisation and parallelisation of the DE model would be needed to make these two models fully overlap in time and space (e.g., to be able to run the DE model on longer time and larger domains and/or to set up a more theoretical test case for the TOPAZ model with much higher temporal and spatial resolution). Because of this lack of overlapping, the analyses have been focused on the analysis of the DE model only and helped us to better understand the diffusion and dispersion properties in the MIZ.

The diffusion analysis explored the dynamics simulated by the DE model in the "collisional" domain. This analysis is robust and shows a clear transition in the integral time scale, reaching a plateau for L>100 m and T>6 h. The dispersion analysis is also statistically significant with several thousand independent float/floes pairs in each $L(0)-\tau$ category.

The analysis performed on the MIZ model and the EVP model in the MIZ areas are much less conclusive, but still provide some interesting information. We noted for example that changing the sea ice rheology from MIZ to EVP does not influence either the absolute value or the growth rate of diffusion. The results also show that decreasing sea ice concentration has a high impact and leads to a significant increase of the absolute value of $\langle r'^2 \rangle$ and K.

4.1.7 Conclusions

The conclusions useful for oil spill modelling in MIZ conditions are the following:

- The averaging scales to be used to extract the fluctuating velocity related to collisions are L=100 m and T=6 h.
- The integral time scale Γ, which may be seen as the memory time or the average time between two collisions, is estimated by the DE model as being about 2 h.
- The absolute diffusivity parameter estimated by the DE model is K~1 m^2/s.
- The standard deviation of the fluctuating speed is about 1.15 cm/s for the DE model (with concentration of 60-70%), whereas it is about 0.46 cm/s from the MIZEX experiment (with concentration of nearly 80%).
- The simulated fluctuating speed has an exponential distribution.
- The diffusion regime in the MIZ is unique and could be seen as a combination of molecular and turbulent diffusion.
- The dispersion rate depends on the initial separation length as $L(0)^{\beta}$ with $0.17<\beta<0.48$.

The robustness of these conclusions should be confirmed by considering variations in ice thickness, floe distribution, and concentration. Such an exercise is expected to give a better understanding of the internal variability of the system, but should not change our qualitative understanding or the order of magnitude of the values already presented.

4.2 D2.2: Diffusion and dispersion in the pack: a comparison between EVP and EB sea ice models and observed buoy trajectories

4.2.1 Reminder of tasks

Task 7.1.1 Implementation of a float tracking module in the NERSC sea ice model

We will implement a Lagrangian floats tracking module in the TOPAZ system. The main goal here is to be capable of tracking thousands of individual sea ice particles. The floats module will initially be applied to the model currently used at NERSC, with EVP and MIZ rheology, before it is applied to new models developed as part of the project or as external contributions. The code will be kept versatile for the future tracking of sea ice tracers that could have their own physics (for example ageing).

Task 7.2.1 Diffusion/Dispersion in the pack using the EVP rheology

We will run simulations over the Arctic basin (at about 10km resolution) and track thousands of floats in the central ice pack over winter, and over summer depending on the available buoy observations. We will perform statistical analyses of both absolute and relative sea ice dispersion from these Lagrangian trajectories, following the methodology presented in Rampal (2008), Rampal (2009b).

Task 7.2.4 Diffusion/Dispersion in the pack using the EB rheology

Diffusion coefficients can be derived from the slope of the diffusion regimes. We will compare the simulated diffusion and dispersion properties as derived with the EVP and EB rheologies to those observed and derived from buoys in the ice pack or in the ocean.

4.2.2 Introduction

A first objective of this task is to describe how to separate the deterministic from the non-deterministic part of the sea ice motion with the theoretical tools developed for turbulent diffusion. Following the turbulent theory of Taylor (1921), Thorndike (1986a) described how to split sea ice motion into a predictable mean part, $\bar{u}$, and a random fluctuating part, u'. The predictable part is forced by the large-scale mean motions in the atmosphere and the ocean, while the random part was suggested by Thorndike (1986a) to be forced by short-term fluctuations in the wind and ocean currents. The fluctuating motion is then analysed to describe the transition from the ballistic to the Brownian diffusion regimes and the absolute diffusivity parameter.

A second objective is to characterise sea ice dispersion. Dispersion describes how two particles move apart in time and is partly the result of accumulated random small-scale motions. Martin(1985) studied sea ice dispersion from a limited set of pairs of buoys deployed on the ice during Arctic field campaigns in the early 80s and found it to be one order of magnitude lower than for the ocean surface. In the case of an oil spill, the dispersion properties indicate how rapidly an oil-infested area spreads in time, and how the dispersion rate depends on the initial size of the infested area.

In addition to the quantification of sea ice diffusion and dispersion from observations, we also analyse the quality of the sea ice motion fields provided by two different numerical sea ice models: the elasto-brittle model (EB) and the TOPAZ model, which uses the common elastic-viscous-plastic (EVP) rheology. We compare synthetic buoy trajectories simulated by the models to real buoy trajectories from the International Arctic buoy Program (IABP) data set. The statistical properties of these trajectories are then analysed to evaluate how the mean drift field and the fluctuating part of the sea ice motion are reproduced by the models.

4.2.3 Data

We use the full 12-hourly IABP positions data set for the 1979-2011 period as reference. For the period 2007 to 2010, we also generate “virtual" buoy trajectories as seen by TOPAZ and by the EB model. The “virtual buoys" are initialized at the same time and position as real IABP buoys, and are “killed" when the real IABP buoy track stops or when the virtual buoy leaves the sea ice according to the model. This gave us three comparable data sets: i) the observed sea ice trajectories, ii) the trajectories of virtual floats as simulated by the EVP sea ice model of TOPAZ, and iii) the trajectories of virtual floats as simulated by the EB sea ice model.

4.2.4 Methods

To perform the diffusion analysis, also called single particle dispersion analysis, we first need to decompose the total sea ice motion into a mean part and a fluctuating part, by using the appropriate temporal and spatial averaging scales *T* and *L*. Figure 14 shows an example of the partition of the displacement of an IABP buoy into the mean and fluctuating parts, $\bar{\mathbf{u}}$ and **u**', respectively. The mean part can be considered homogeneous and stationary at time and spatial scales smaller or equal to *T* and *L*, whereas the fluctuating part contains the quasi stochastic part linked to turbulent and small scale motion (i.e. oceanic eddies or inertial motion) and to the succession of atmospheric perturbations.

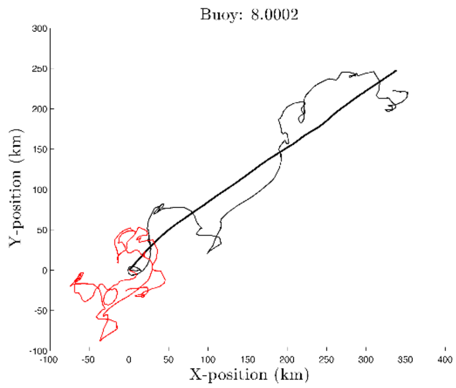

Figure 14: Example IABP buoy 8.0002 to show the partition onto a mean and fluctuation part of the motion, the measured displacement from its original position (thin black), mean displacement from $\bar{u}$ (thick black), fluctuating displacement from *u'* (red).

For each buoy trajectory we then compute the fluctuating sea ice displacement from the fluctuating velocities, *u*' and *v*', as

$$r'_x(t) = r'_x(t - \Delta t) + u'(t)\Delta t \qquad (2)$$

$$r'_y(t) = r'_y(t - \Delta t) + v'(t)\Delta t \qquad (3)$$

where Δt is the time step in the data set and $r'_x(t=0)=0$ and $r'_y(t=0)=0$.

The square root of $\langle r'^2(t)\rangle$ (i.e. the standard deviation of the fluctuating displacement) may be used to estimate how the radius of search around the trajectory predicted by the mean drift should evolve in time. When the fluctuating displacement distributions are in the Gaussian attraction basin, the probability of finding a particular trajectory within a circle of radius 1, 2 and 3 standard deviations around the mean trajectory is about 68, 95 and 99.7%, respectively.

Finally, the analysis of the fluctuating displacements also provides an estimation of the absolute diffusivity *K*. If the medium behaves like a turbulent fluid, the information on the mean drift and the absolute diffusivity can be used directly to predict the spread of pollutants, nutrients, and any passive tracer *C* moving within this medium. For example, one can use the classical advection-diffusion equation:

$$C_t + \bar{\boldsymbol{u}} \cdot \nabla C = \nabla \cdot (K \nabla C) \qquad (4)$$

where $\bar{\boldsymbol{u}}$ is the mean velocity field defined with the right averaging scales and *K* is the corresponding diffusivity field or constant parameter.

In addition to the diffusion analysis, we also performed a dispersion analysis, also called multiple particle dispersion. This type of analysis is widely used in oceanography and is mainly based on the analysis of drifter motions. Relative dispersion describes how two particles move apart from each other through time (Martin1985, Rampal2008). Following a pair of buoys, dispersion is defined as the change in separation (or distance between two buoys) *L* after a time τ as

$$\Delta r = ||L(\tau) - L(0)|| \qquad (5)$$

4.2.5 Results

For the diffusion analysis, we performed the same sensitivity analysis to the averaging scales as Rampal (2009b) for the limited period 2007 to 2010. We found the same values for *L*=400 km and *T*=165 days, which are then used to define the mean sea ice drift for all the analyses performed in this study.

The two main features in the mean sea ice drift are the Beaufort Gyre and the Transpolar drift. The strength and the size of the Beaufort Gyre, as well as the strength of the Transpolar drift, vary from one year to the other. The TOPAZ model generally overestimates the mean field and does not correctly reproduce the spatial patterns. In particular, the size of the Beaufort Gyre is often overestimated and the model does not reproduce the low velocities in the southern part of the Beaufort Gyre, towards the Canadian Arctic Archipelago (see figure 5). The mean ice drift simulated by the EB model is much more similar to observations than is that of TOPAZ. The EB model represents well the patterns of the mean ice drift like the Beaufort Gyre, the Transpolar drift and the very low velocities along the Canadian Arctic Archipelago.

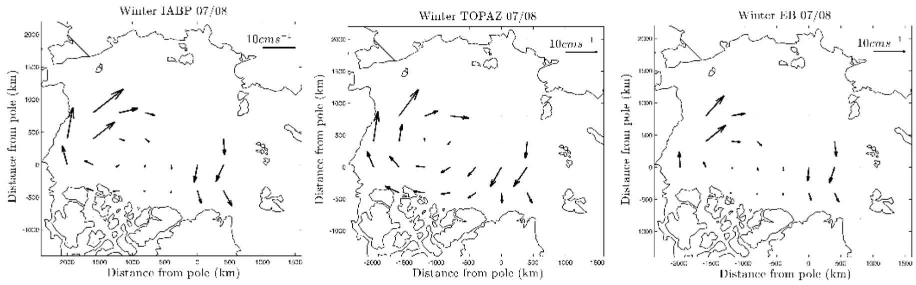

Figure 15: Mean velocity for IABP (left), TOPAZ (center), and EB (right) for the winter 2007/2008 interpolated onto a 400x400 km regular grid, with coordinates $(\hat{\boldsymbol{x}}, \hat{\boldsymbol{y}})$. For each grid point $(\hat{\boldsymbol{x}}, \hat{\boldsymbol{y}})$, the plotted vector is the weighted average of the mean velocity of all the buoys within a L/2 radius. The applied weight is $\boldsymbol{w} = \boldsymbol{e}^{-\boldsymbol{r}^2/(2\boldsymbol{L}^2)}$ where $\boldsymbol{r}$ is the distance between the buoy and the grid point (i.e. $\boldsymbol{r} = \sqrt{(\mathbf{x}-\hat{\boldsymbol{x}})^2 + (\mathbf{y}-\hat{\boldsymbol{y}})^2}$).

The mean speed distribution from observations fits well with an exponential distribution with a mean value of the mean drift equal to 2.45 cm/s. TOPAZ does not produce an exponential but rather a Gaussian distribution with a mean value equal to 3.38 cm/s. The mean velocities from the EB model are slightly lower compared to the IABP data but follow closely an exponential fit with a mean value equal to 2.00 cm/s. As a conclusion, the TOPAZ model overestimates the mean ice drift by about 38%, whereas EB underestimates the mean drift by about 18%.

The distribution of the fluctuating speed from the IABP data closely follows an exponential fit with a mean fluctuating speed equal to 6.9 cm/s. The fluctuating velocities from TOPAZ are too high (by about 30%) with a mean value equal to 8.97 cm/s, do not follow an exponential distribution and miss the highest values of fluctuating speed. The fluctuating speeds from EB are slightly too low (by about 10%) with a mean value equal to 6.14 cm/s and follow an exponential distribution within the range 0 to 30 cm/s. The EB model also misses the highest values of sea ice speed.

Another way of analyzing the fluctuating displacement is to look at the variance as a function of time $\langle r'^2(t)\rangle$ (see figure 16). Both the EVP sea ice rheology in the TOPAZ system as well as the EB rheology represent the initial "ballistic regime" where the displacement grows proportional to t^2 ($\langle r'^2(t)\rangle \sim t^2$) and the later "Brownian" regime where the displacement grows proportional to t ($\langle r'^2(t)\rangle \sim t$). This transition occurs around the integral time scale Γ=1.3 days. However, the absolute value of the variance is largely overestimated by the TOPAZ model. The EB results exhibit a fluctuating displacement variance very close to the one derived from observations.

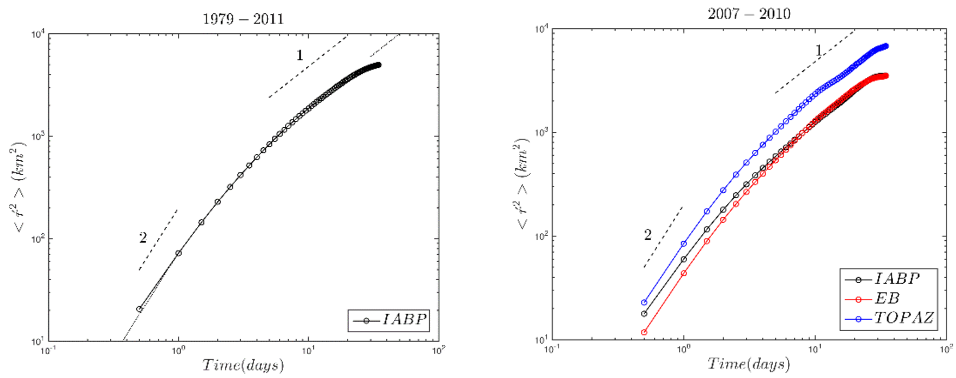

Figure 16: Ensemble mean of the variance of the fluctuating displacement <r'2> for the winter seasons 1979-2011 (left panel) and 2007-2011 (right panel). The stippled lines show the theoretical slope for the initial "ballistic" and later "Brownian" regimes. The dotted lines on the left panel correspond to the asymptotic solution of the equations 8 and 9 of Deliverable 2.2.

The variance of *r*' is crucial information for operators in Arctic sea ice, as it gives an estimate of how the size of the search area around the predicted mean drift should evolve through time. If an operator can only trust the mean drift (this is the case for forecasts longer than a few days), the search area could be defined as a circular region with a radius depending on the standard deviation of the fluctuating displacement. We verified that about 68.9%, 95.9% and 99.6% of the fluctuating displacements are smaller than 1, 2 and 3 standard deviations, respectively. Another way of interpreting the same information is to define the search radius as a function of the standard deviation $\sqrt{\langle r'^2(t) \rangle}$. Looking at the IABP data for the period 1979 to 2011, we can for example estimate that the search radius (defined here as equal to 3 standard deviations) should be about 87 km after 5 days (corresponding to a surface area of 24.000 km^2), and about 206 km after 30 days (corresponding to a surface area of 134,000 km^2). As the mean speed and deformation in the Central Arctic are increasing (Rampal2009a), we would expect higher values for recent and coming years.

As in Martin(1985), we showed that the rate of dispersion, defined as $\langle \Delta r^2 \rangle \tau^{-1}$ varies as $\langle \Delta r^2 \rangle \tau^{-1} \sim L(0)^{1.8}$, meaning that the dispersion rate decreases much more rapidly towards smaller scales than in the case of oceanic surface turbulence, for which the exponent would be around 1.

The magnitude of the dispersion rate is an important information in case of oil spill in ice-covered area, as it may indicate how the size of the oil spill changes in time. The change of size can be estimated by the standard deviation of Δr for a given time τ. For oil spills of about 10 km, the standard deviation $\sqrt{<\Delta r^2>}$ is about 2.6 and 4.2 km after 1 and 10 days, respectively. For oil spills of about 300 km, the change of size would rather be about 30 and 130 km, after 1 and 10 days, respectively. Finally, even if the underlying processes may be different at small and large scales, the results agree on a relative change of size of about 40% after a period of 10 days.

The comparison of the models in terms of dispersion has a much lower degree of confidence due to the small number of pairs of buoys available during the 3 winters analysed in this report. For the model comparison, only the dispersion analysis for an initial separation length of about 300 km has sufficient data to be conclusive. This limited analysis indicates that the two models underestimate the dispersion at this scale.

4.2.6 Conclusions

Operational oil spill trajectory modelling is limited by the growing uncertainty coming from the non-deterministic part of the motion of the surrounding medium. Applying Taylor's diffusion theory to sea ice allowed us to properly separate the mean/deterministic part from the fluctuating/non-deterministic part of the sea ice motion, and to quantify the sea ice diffusivity parameter. The estimation of the mean drift velocity and diffusivity could be used directly to estimate the most probable position of the ice over time scales longer than a few days, and more importantly the uncertainty around this position. This information may also be used to prepare oil spill responses. In particular, the standard deviation of the fluctuating displacement may be used to determine the appropriate radius of the search area.

Oil spill modelers also need reliable information about how sea ice disperses and deforms in time. We showed that the rate of dispersion is one order of magnitude smaller than for the ocean surface for the same $L(0)$ and varies as a power-law function of the initial separation length with an exponent 1.8, instead of 1 for ocean surface.

Finally, diffusion and dispersion analyses showed that the EB model performs much better than the TOPAZ model and is able to provide realistic sea ice trajectories with the right diffusion properties. Reproducing these statistical properties is crucial when using such dynamical models to force oil spill models.

CHAPTER 5. WP3: UNCERTAINTIES

5.1 D3.1: Remote sensing for regional scale model initialisation

5.1.1 Reminder of tasks

Task 7.3.2 Remote sensing for regional scale model initialisation

- *Part 1: Lead detection from near 90 GHz satellite radiometry: Within the consortium, a lead detection algorithm using the 89 GHz channels of the AMSR-E microwave radiometer was developed by Rohrs2012, and initial data are already available for task 7.3.3. As the AMSR-E sensor is not in operation any more this algorithm will be adapted to the 92 GHz channels of the SSMI/S instrument on the DMSP F17 and F18 satellites, whose data are currently available. Compared to AMSR-E the SSMIS instrument has a lower spatial resolution of about 15 km. If data from the AMSR2 sensor on the Japanese SHIZUKU satellite becomes publicly available during the project period, the algorithm will be also adapted for this dataset. Although this algorithm is optimised for lead detection, it does not give thin ice concentration for polynya areas and also underestimates the total lead area. Within the project, improvements of the algorithm will be tested by optimizing the algorithm tie-points and combining it with other thin ice retrieval algorithms optimised for polynyas (Kern2007).*
- *Part 2: Lead/ridge identification from SAR and optical satellite observations: Lead and ridge statistics can potentially be derived from SAR or optical satellite sensors like MODIS with high spatial resolution (10 m to 1 km). However, due to the dependence on clouds and daylight (MODIS), and limited data availability (Radarsat SAR) the temporal and spatial resolution of such products will vary and cannot be guaranteed for an operational application.*

  Selected cloud free MODIS images will be used to classify thin ice/open water lead areas using a reflectance threshold Rohrs2012. Heavily deformed ridges stand out with high backscatter values in SAR data (Dierking2006b). Selected Radarsat wide swath mode scenes will be used to identify large-scale ridges and deformation areas. Methods to extract ridge areas from SAR data are under research and will be assessed. Alternatively, ridge areas can be extracted manually for selected scenes.

  The different impacts of the daily, low-resolution lead dataset compiled under part 1 in comparison to the higher resolution ridge dataset on the model performance can be evaluated.

5.1.2 Introduction

Leads are prominent features covered with thin ice or open water within the sea ice cover. In the context of this project, they represent locations of reduced mechanical strength, which are needed to initialise the elasto-brittle sea ice model. To this end, we implement an algorithm to obtain Arctic-wide lead fraction from the microwave satellite radiometer AMSR2. Here a daily time series of thin ice concentration (or lead fraction) from January 2013 to December 2014 is calculated on a 5 km grid. We also validate these results against higher resolution SAR data. Visual inspection of SAR images gives a more accurate estimate of lead location and size, but automatic lead detection using SAR remains a challenge.

5.1.3 Lead and thin-ice detection from AMSR2 89 GHZ data

Sea ice information has been obtained from space-borne microwave radiometers for more than 30 years (Cavalieri1994). Satellite radiometry offers the advantage of daily complete coverage of the polar regions, and an independence of light and clouds. The most commonly used sea ice parameter derived from passive microwave (PMW) radiometry is sea ice concentration, but here we will focus on the observations of the area covered by thin ice and leads.

The biggest disadvantage of PMW satellite measurements is their low spatial resolution, which particularly affects our ability to detect narrow leads. There are two possibilities to improve the spatial resolution of PMW based observations: a) increase the antenna size and b) increase the frequency used for the observations. The Japanese Advanced Microwave Scanning Radiometer - Earth Observation System (AMSR-E) launched in 2002 on NASA's Aqua satellite has a bigger antenna than its predecessors, improving the spatial resolution of all channels by a factor of about two. Spreen (2008) demonstrate that the AMSR-E 89 GHz channels can be used to retrieve sea ice concentration with a comparable quality to the traditionally used 19/37 GHz channel combination. This again improves the spatial resolution by a factor more than two and sea ice concentrations can be obtained daily and globally with about 5 km resolution from AMSR-E.

Rohrs (2012) used the ratio of the 19 and 89 GHz AMSR-E channels to obtain the thin ice concentration of leads within the ice pack. AMSR-E ceased operation in October 2011 and these datasets ended. Since July 2012 PMW measurements from the AMSR2 radiometer on board the Japanese GCOM-W1 satellite became available. AMSR2 offers similar frequency channels and resolutions as AMSR-E. We base our work on the algorithm presented by Rohrs2012, adapt it to AMSR2, and calculate a 2-year long time series from January 2013 to December 2014 of thin ice concentration in leads.

The main idea of the Rohrs2012 algorithm is to use the unique radiometric signatures of thin ice in the brightness temperature (TB) ratio between the 89 GHz and 19 GHz channels to detect thin ice areas in the ice cover. The algorithm is optimised to detect leads (elongated features), not polynyas. In winter time, when almost all leads are ice covered the derived thin ice concentration (TIC) can therefore also be considered as a lead fraction. In the summer months, when leads stay open TIC and lead fraction are not interchangeable. The algorithm will however classify open water in leads as thin ice, as long the open water fraction stays below a given threshold. We can therefore use both terms TIC and lead fraction interchangeably in the summer as well. Due to surface melt and an ice concentration cut-off threshold, we expected larger uncertainties during the summer months, but these are not assessed here. The algorithm can be divided into 3 steps:

1. **Calculation of the ratio between the 89 GHz and 19 GHz channels:** Neglecting the atmospheric influence one can assume that the TB 89 GHz V to 19 GHz ratio is sensitive to thin sea ice. In order to calculate this ratio the TB 19 GHz 10 km data is interpolated onto the 5 km grid of 89 GHz channels.
2. **Spatial filtering:** A spatial filter is applied to separate the surface from the atmospheric signal due to their different spatial scales, and to enhance the signal of the leads.

3. **Definition of thin ice concentration (TIC):** Leads are recognised by their thin ice cover. Analogue to sea ice concentration, a thin ice concentration (TIC) is defined to describe the area fraction of thin ice compared to other ice classes.

These steps are implemented for the daily AMSR2 TB fields. In addition, a sea ice concentration cut-off of 10% is applied removing some spurious open water TIC classification in the marginal ice zone (MIZ). As a last step, a land mask is applied. This process results in daily average 1520×2240 maps.

5.1.4 Results

Linear features of high TIC (leads) are present in most of the TIC maps. Figure 7 shows four daily maps of the AMSR2 TIC/lead fraction fields. These show extensive fracturing in the Beaufort Sea, the Canadian Basin, and the Fram Strait, which are well known to be areas of extensive lead formation (Brohan2014, Beitsch2014). The leads in the Fram and Nares Straits often form arches and the development and disintegration of these ice arches can be used as an indicator for large changes in sea ice through flow (Kwok2010b).

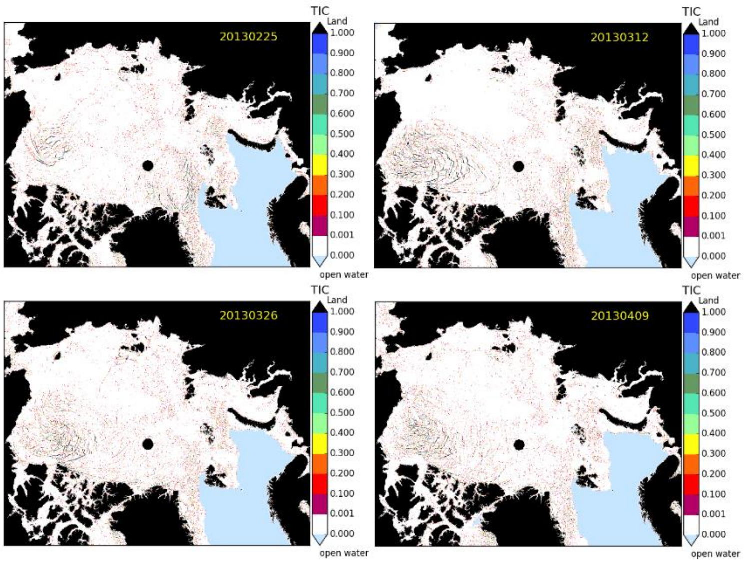

Figure 17: Time series of AMSR2 TIC/lead fraction from 25.2.2013 (upper left) to 9.4.2013 (lower right). During this time period, a strong sea ice-fracturing event in the Beaufort Sea and Canadian Basin can be observed.

To assess the quality of the AMSR2 TIC product we compare it against Radarsat-2 wide-swath mode SAR data with 100 m resolution. Automated identification of leads in the SAR images is very difficult, but due to their shape leads can, in general, be reliably identified by visual inspection. In eleven SAR scenes from 10 different day clear lead patterns could be identified and were compared to the AMSR2 TIC data of the same day. An example is shown in figure 18.

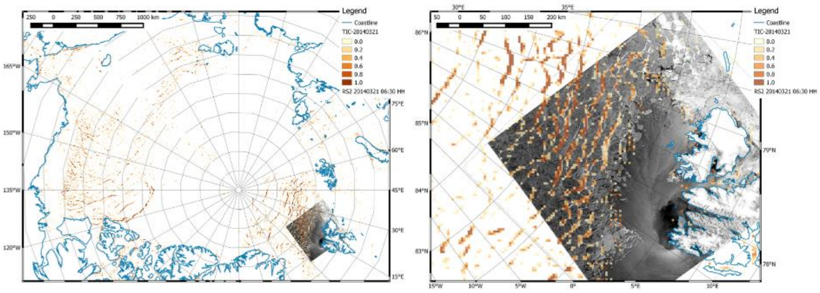

Figure 18: AMSR2 thin ice concentration in the Arctic Ocean on 2014-03-21 with 5 km spatial resolution (left). A comparison to higher resolution Radarsat-2 SAR data (right) shows good agreement but also an underestimation of identified lead area, e.g., between 81–82N, 30–35E. AMSR2 data provided by Jaxa. Radarsat-2 images provided by NSC/KSAT under the Norwegian-Canadian RADARSAT agreement 2013 ©MacDonald, Dettwiler and Associates)

The general structure and location of leads is well identified in the AMSR2 TIC data, when compared with the SAR images. The TIC concentration appears also to be meaningful in most cases, with larger and wider leads having higher TIC values. Smaller leads are not identified in the AMSR2 TIC data, with nearly all leads narrower than 500 m and some leads up to 2 km wide not identified. This leads to an underestimation of lead area of about 30-40%. For comparison Rohrs2012 assessed the underestimation of their AMSR-E lead data to be 50%, based mainly on comparison to visual MODIS data. We therefore estimate the classification result in our examples to be slightly better than theirs.

Open water areas in the MIZ tend to be incorrectly classified as leads leading to a local lead area overestimation there. This problem can be improved by applying a higher ice concentration threshold than the 10% used here. A higher threshold on the other hand has the disadvantage that during summer more open water leads will not be identified by the algorithm.

Overall, the SAR comparison confirms that the AMSR2 TIC algorithm implementation works as expected and is at least as good as the preceding AMSR-E TIC data.

5.1.5 Conclusions

AMSR2 data can be successfully used to determine the major lead systems within the Arctic basin. Comparison with higher resolution SAR data shows good agreement in lead locations. Smaller leads (below 500 m wide) are in most of the cases not identified, which leads to an underestimation of the total lead area. The ten SAR scenes used for evaluation here are not enough to make a clear recommendation for the thin ice concentration (TIC) accuracy. In most of the cases good agreement between TIC and the size of the lead in the SAR data is observed. Overall, however, it is estimated that the total lead area is underestimated by 30-40% due to the missing leads in the TIC results. This is in accordance with previous studies.

The higher resolution SAR data shows promises for more accurate lead detection. SAR data cannot cover the complete Arctic on a daily basis and automatic, unsupervised classification still remains a challenge. For operational, near-real time model initialisation for short-term sea ice forecast the 5 km resolution Arctic-wide AMSR2 lead fraction fields are deemed a good choice.

5.2 D3.2: Sensitivity of the EB sea-ice model to initial conditions and ice mechanical parameters

5.2.1 Reminder of tasks

Task 7.3.3 Sensitivity of the EB sea ice model to initial conditions and ice mechanical parameters
The sensitivity of the ice velocity field produced by the EB rheology to the initial ice conditions and to the model parameters will be evaluated in the Kara Sea and Arctic configurations. To estimate the influence of the initial conditions, we will use the maps of leads provided by Rohrs2012 (also see Task 7.3.2) to define the initial level of damage in the ice cover. In addition, we plan to explore the dependence of our simulation results with EB on different ice mechanical parameters such as the cohesion and the Young modulus.

5.2.2 Introduction

Dispersion in sea ice is directly related to its deformation/fracturing. For example, Rampal (2008) analysed buoy dispersion to characterise the scaling properties of sea ice deformation. Understanding the sensitivity of the simulated sea ice deformation to the model parameters and initial conditions will then directly help us to improve the representation of sea ice absolute and relative dispersion, which is one of the main objectives of this project.

Sea ice dynamics also strongly depend on the external forcing. The simulated sea ice drift is especially sensitive to the atmospheric forcing and to the parametrisation of the surface wind drag. We propose an innovative method to calibrate the air drag coefficient. This calibration is performed for two different sets of wind forcing, the ASR and ERA-interim datasets. The comparison of the results obtained with the two forcing sets allows us to investigate the sensitivity of the simulated sea ice drift to the wind forcing.

In shallow water areas, sea ice may be grounded, meaning that sea ice keels (i.e. the underwater part of the ridges) are in contact with the sea floor and therefore stop or drastically reduce the ice motion. This effect contributes to the formation and persistence of land fast ice (i.e. non-moving ice grounded or stuck to the coast). Reproducing the land fast ice formation, position and breakup may be useful, for example to help operators navigating in ice-covered shallow water areas.

5.2.3 Sensitivity analysis of the simulated deformation fields

To analyse the sensitivity of the simulated sea ice deformation to model parameters and initial conditions, we use the Arctic configuration that has been presented in Deliverable 1.2. In this sensitivity study, sea ice thermodynamics is not taken into account and the healing term is deactivated in the simulations presented here by setting the damage relaxation time to a very large value.

Two different initial conditions are used: either the sea ice concentration A_{topaz} from the TOPAZ reanalysis or the sea ice concentration A_{obs} from observations. A_{obs} is defined as a combination of the sea ice concentration and lead area fraction fields coming from two different datasets: the AMSR-E/ASI sea ice concentration, here denoted A_{tot} (http://www.iup.uni-bremen.de/seaice/amsr/, University of Bremen, Bremen, Germany, October 2011) and the AMSR-E lead area fraction, produced with the same method as the one presented in Deliverable

3.1. A_{lead} and A_{tot} provide different information. A_{lead} identifies the narrow leads in high concentration areas from anomalies in the brightness temperature ratio whereas A_{tot} provides the smooth background concentration fields and may also identify large open water areas such as polynyas. When using the two different initial conditions, A_{obs} and A_{tot}, we found similar distributions of deformation, and almost identical values for the total opening, closing and shearing rates. In both cases, results exhibit a strong spatial localisation and similar statistical properties, meaning that this characteristic of the model is not inherited from initial conditions but rather generated by the model itself.

The sensitivity of the model to the value of the Young modulus Y, compactness parameter α, and cohesion c has also been evaluated. The sensitivity analysis shows that the degree of multifractality of the sea ice deformation scaling invariance is mainly controlled by the cohesion parameter c. The compactness parameter α mainly impacts the total opening and closing rate with minor impact on the total shear rate. From this analysis and other experiments not presented in this report, an optimal set of parameters is defined. The compactness parameter α is set to -40, the time step Δt to 200 s and the Young modulus to 9 GPa. For this set-up the cohesion c is set to 4 kPa, the maximal tensile stress σ_{Nmax} is set to $\frac{5}{4}c$ and the maximum compressive stress σ_{Nmin} is set to –80 kPa.

5.2.4 Calibration of the air drag parameter and sensitivity to the wind forcing

When internal stress is negligible, sea ice moves in free drift mode and the stationary solution of the momentum equation is then:

$$\boldsymbol{u} = \boldsymbol{u}_w + Na\,\boldsymbol{u}_a \qquad (6)$$

where u, u_a and u_w are sea ice, air and ocean velocities, respectively, and $Na = \sqrt{\rho_a c_a / \rho_w c_w}$ is the Nansen number (ρ_a and ρ_w are the air and seawater densities, respectively, and c_a and c_w are the air and water drag coefficients, respectively). The first estimate of this number ($Na \approx 2\%$) was made by Fridtjof Nansen during the Fram expedition (1893-1896) by comparing the drift of his boat, when trapped in the ice, to local wind and ocean velocities. The air and water density being considered as constant, the Nansen number only depends on the ratio between the two drag coefficients, c_a and c_w.

In the literature, different tuning experiments have led to different values for the Nansen number. For example, Massonet2014 estimated that the optimal value for the Nansen number was equal to 2.5% for the NEMO-LIM3 model forced by NCEP/NCAR winds (analysed period: winter seasons 2007 and 2012). Kreyscher (2000) also found a value of 2.5% for their VP model forced by ECMWF winds (analysed period: 1979-1994). Miller (2006) found for the CICE sea ice model forced by ECMWF winds different values ranging from 1% to 2% (analysed period: 1994-2001). All these analyses compared the simulated and observed sea ice drift over the whole Arctic basin with no constraints on sea ice being in free drift or not, leading to a strong interdependence between the calibration of the mechanical parameters and the calibration of the drag coefficients. To circumvent this issue and to provide optimal air drag coefficients that are independent of the mechanical parameters, we propose here to calibrate the air drag coefficient only for conditions corresponding to free drift. Despite its simplicity, such a method has never been presented in the literature, to our knowledge. Moreover, it may be easily applied to any kind of sea ice model, whatever the rheology or the numerical implementation.

The calibration is performed for the winter season 2007-2008 (from end of October to end of April) and is based on the sea ice drift data provided by the GlobICE project (http://www.globice.info). Sea ice drift vectors are computed when two successive SAR images from the ENVISAT satellite are available and treated by the tracking algorithm. The time interval between two images is typically 3 days. The drift vectors are given on a regular grid having a resolution of 5 km.

The scatter plots corresponding to the non-optimised and optimised solution are shown in figure 19. For the non-optimised case, the best fits are u_{obs}=1.49u_{fd}+0.4 and v_{obs}=1.42v_{fd}+0.4, meaning that there is no significant constant bias, but that there is a strong and systematic underestimation of the simulated drift. For the optimised case (obtained by multiplying the Nansen number by a factor 1.4), the best fits are u_{obs}=1.07u_{fd}+0.3 and v_{obs}=0.98v_{fd}–0.4, meaning that there is still no constant bias, but that the simulated drift now fits very well with the observations, as the 1st order coefficients are very close to 1 for the two components. In all the cases, the norm of the residuals of the linear fit (i.e. the root mean square distance between the blue points and the red line) is similar and about 160 km/day. This value is not reduced by the calibration of the drag, meaning that this error comes from the forcing itself and from unresolved processes (i.e. local or intermittent unresolved winds and currents, collisions between floes, etc.). By calibrating the air drag coefficient, the mean error for the free drift velocities is reduced from 5.7 to 3.8 km/day and the median error is reduced from 5.3 to 3.2 km/day. The correction of the systematic underestimation of the ice velocity induces a constant shift of the entire cumulative distribution of errors to lower values.

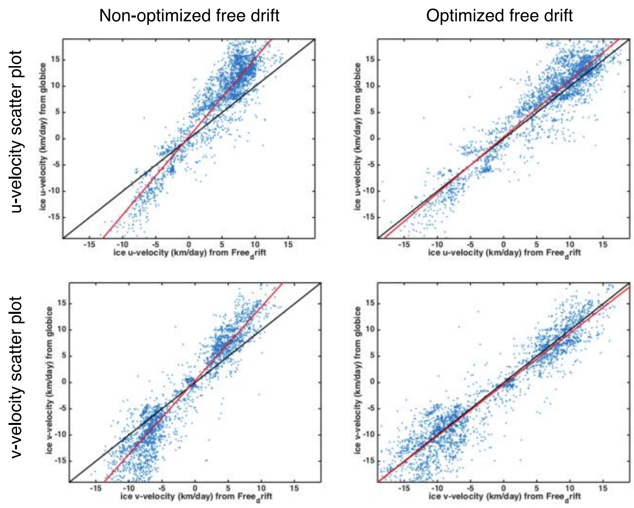

Figure 19: Scatter plots for the u-component (first line) and v-component (second line) of the free drift velocities obtained from observations versus non-optimised solution (left) and from observations versus optimized solution (right). The red lines correspond to the best linear fit in a least-squares sense for each component.

The optimal Nansen number for ASR winds is found to be *Na*=4.2%. In our case (i.e. with c_w =0.0055), it corresponds to setting the air drag coefficient to c_a=0.0076. This optimal value of the Nansen number is higher than the classical values. This is consistent with the fact that ASR surface winds are weaker than, for instance the geostrophic winds and then the surface wind of ERA-interim produced by ECMWF (Bromwich2015).

We did the same exercise for the ERA-interim winds, which are frequently used to force large-scale sea ice models. It is interesting to compare the errors obtained with the two different forcing fields, ASR and ERA-interim. We note that after calibration the constant biases and also the residuals of the linear fits are significantly higher with ERA-interim (Biases: 2.1 and 0.8 km/day; RMS: 218, 176, 220 and 165 km/day, median error: 4.8 km/day) compared to ASR (Biases: 0.3 and -0.4 km/day; RMS:160 km/day, median error: 3.2 km/day). This indicates that ASR surface winds are better than ERA-interim surface winds. This is consistent with previous studies (Bromwich2015) and with the fact the ASR reanalysis has a higher spatial and temporal resolution and assimilates more remote and in-situ observations.

Since the calibration is independent of the mechanical parameters, the optimised air drag parameter could also be directly used in other standalone sea ice models running with the same external forcing and drag parametrisations. The optimal drag coefficient could also be directly used for oil spill models based on Equation 6, and it may drastically improve the simulated ice/oil motion where the ice moves in free drift. For coupled ice–ocean systems, however, our numbers should not be used directly and the calibration should be repeated to take into account the feedbacks involving, for example, the oceanic surface currents.

5.2.5 Basal stress parametrisation

Most sea ice models do not take into account the grounding effect and are thus incapable of correctly reproducing sea ice drift in shallow water areas (see figure 20 for an example of the elasto-brittle (EB) model without the basal stress). To correct this issue, we implemented the basal stress parametrisation for modelling land fast ice proposed by Lemieux (2015) (see example shown in figure20). In their study, the parametrisation is validated against fast ice observations over several winter seasons. We use the same parameter values except for the maximum basal stress parameter, for which their value (15 N/m^3) is adapted to be consistent with our value of the air drag coefficient. The maximum basal stress parameter value (in N/m^3) is then set to 15 $c_a/c_a^{Lemieux}$. In our case, the topography comes from the 1 arc-minute ETOPO1 global relief model (amante2009egrm). Another minor difference compared to Lemieux (2015) is that we also take into account the sea surface elevation given by TOPAZ to evaluate the water column height.

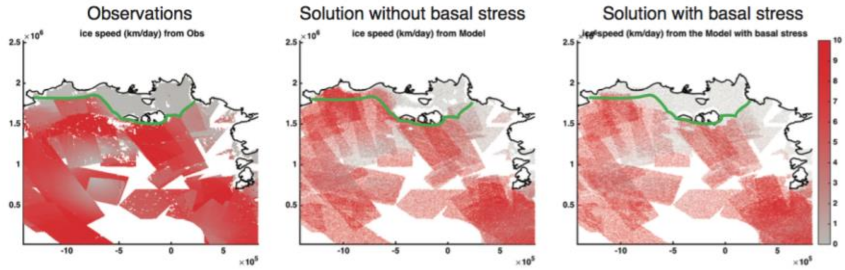

Figure 20: Example of detection and simulation of the grounded sea ice in Laptev Sea. Left: Observed sea ice speed for the period 5-14 March 2008. The green line is a handmade estimate of the position of the fast ice edge based on the observed sea ice speed. Centre: Sea ice speed simulated by the model with optimized air drag parameters but without the basal stress parametrisation. The simulated velocity is built to match the observation in space and time. Right: Sea ice speed simulated by the model with the basal stress parametrisation. The domain and initial conditions are not exactly the same for the two simulations, it may have an impact but has not been analysed. The comparison made here is purely illustrative.

5.2.6 Conclusions

The EB model produces sea ice deformation fields showing similar statistical signatures as those found for the Arctic sea ice cover, in particular a multifractal spatial scaling invariance. These statistical properties do not rely on the realism of the initial concentration and thickness fields but rather emerge from the sea ice rheological model. We quantified how the deformation simulated by the EB model is sensitive to the mechanical parameters and initial conditions, and used this to define an optimal set of mechanical parameters. We proposed an innovative method to calibrate the drag parameters. This calibration reduces significantly the differences between the simulated and observed sea ice drift. Another benefit of this calibration is that it provides optimal values for the drag parameters and the Nansen number that could be directly used in oil spill models when the ice moves in free-drift conditions. Finally, results of the EB model with and without basal stress parametrisation are presented to show the interest of having such a parametrisation to correctly reproduce sea ice drift near the coasts and in shallow water areas.

5.3 D3.3: Evaluation of the uncertainty by ensemble simulations

5.3.1 Reminder of tasks

Task 7.3.1 Evaluation of the uncertainty by ensemble simulations

To be able to evaluate uncertainties in trajectories calculated by particle tracking methods, we will take advantage of the advanced ensemble methods incorporated in the TOPAZ system (sak12b). Here we will use random perturbation of the initial conditions and the time dependent atmospheric forcing fields. A spectral method is used to generate random perturbations at given spatial and temporal scales (eve03a, cou09b). First, we will apply these methods in the coupled ice–ocean model currently used at NERSC and running in both the pack and the marginal ice zone. If possible, we will also apply these methods to the future version of our coupled model that will include the EB rheology. Uncertainties in the predicted trajectories will be estimated by looking at the spread after 1 day, 3 days and a week (mel12).

5.3.2 Introduction

In this deliverable, we evaluate the uncertainties in ice drift forecast trajectories as a function of the forecast horizon. Four representative areas of the Arctic have been selected where a large number of synthetic floats have been deployed in each member of an ensemble of probabilistic forecasts, produced by the TOPAZ system (which uses the EVP sea ice rheology). The results are summarized in Table 1. The present study considers the effect of uncertainties arising from random errors in atmospheric and ocean forcing on the trajectories and is complementary to the studies of physical dispersion and diffusion in sea ice from the D2.1 and D2.2 deliverables (see sections **Error! Reference source not found.** and **Error! Reference source not found.**) and to the sensitivity to the air drag coefficient presented in D3.2 deliverable (see section **Error! Reference source not found.**). It is the first time that such a probabilistic numerical forecast is attempted for sea ice drift and there is therefore no scientific or technical literature available for comparison. An analogous study has been performed with the same TOPAZ system for surface currents in the open ocean (North Atlantic) by Melsom (2012). Its adequate performance in the open ocean (within 30%) is an indication that the ensemble generation routines and the errors applied to the winds are reasonable and should a priori be useful on ice-covered waters too. This will unfortunately be contradicted by the results presented below but also indicate a way forward in sea ice drift forecasting.

5.3.3 Experiment design

TOPAZ4 is the latest version of TOPAZ, a coupled ocean-sea ice data assimilation (DA) system for the North Atlantic Ocean and Arctic. The system is based on an ensemble Kalman filter (EnKF) (Eversen1994a) with a 100-member ensemble. It uses the hybrid coordinate ocean model (Bleck2002, Chassignet2006) coupled with a classical Elastic-Viscous Plastic sea ice model (Hunke1997). TOPAZ uses here version 2.2.12 of HYCOM. The model is coupled to a one-thickness category sea ice model with elastic-viscous-plastic (EVP) rheology (Hunke1997); its thermodynamics are described in Drange (1996) with a correction of heat fluxes for sub-grid scale ice thickness heterogeneities following Fichefet (1997). The model domain covers the North Atlantic and Arctic basins, with the horizontal model grid created by a conformal mapping with the poles shifted to the opposite side of the globe to achieve a quasi-homogeneous grid size (Bentsen1999). The grid has 880×800 horizontal grid points, with approximately 12-16 km grid spacing and an increased resolution towards the North Pole. For the experiment presented here, TOPAZ is forced at the ocean surface with fluxes derived from 6-hourly reanalyzed atmospheric fluxes from ERA-interim (Dee2011), which has a resolution of 0.25^{o}.

The model perturbation system is a critically important part of TOPAZ as it determines the quality of forecast error covariance and therefore the success of data assimilation. It accounts for the model error by increasing the model spread through perturbation of a number of forcing fields. The perturbations are computed in a Fourier space with a decorrelation time-scale of 2 days and horizontal decorrelation length scale of 250 km. We perturb air temperature, with the standard deviation of 3^{o}C; cloud cover (20%); and per-area precipitation flux (30%). The perturbations of the wind field are derived from sea level pressure (SLP) perturbations, which have a standard deviation of 3.2 mb decorrelation lengths and time scale identical to the previous perturbations. The wind perturbations are the geostrophic winds related to the SLP perturbations, their intensity being inversely proportional to the value of the Coriolis parameter. At 40^{o}N the standard deviations of the winds is 1.5 m/s.

For the experiments performed here, the TOPAZ model was initialized from a single restart file extracted from the MyOcean reanalysis on 8th February 2008. Ten members were then spun up for 21 days with perturbations of the surface boundary conditions as described above. The three-week spin up time corresponds to the typical time scale for these perturbations to grow into sufficiently large deviations of ocean surface currents and ice drift in the TOPAZ model. The following ensemble forecast period then covers one week from the 1st to the 8th March 2008. Model outputs are saved from each member of the ensemble at an hourly frequency to be used as input to the Lagrangian drifter module.

We selected sampling boxes in four areas of interest of the Arctic, each 200 by 200 km (see figure 21):

- The Barents Sea close to the ice edge. Thin ice.
- The Kara Sea. Thin ice but pack ice.
- The Beaufort Sea. Thick pack ice.
- The Transpolar Drift, as a region where the sea ice drift regime differs from the previous three areas. Thick pack ice.

In all areas, the ice concentration is at its maximum allowed value in the model (99%) so the dependency on ice concentration has not been evaluated. In particular, trajectories in the Marginal Ice Zone have a limited lifetime and their statistical analysis would have suffered from the "survivor bias". We expect however, that lower ice concentration would increase the ice mobility and therefore the trajectory uncertainty. In each box 100 trajectories are initialised, regularly spaced in an array of 10×10 synthetic floats. The spacing between the floats is 20 km (about the width of 2 TOPAZ model grid cells) so that — accounting for the numerical dependency of neighboring grid cells in TOPAZ — the smallest scales resolved by the model contribute to the spatial variability of the uncertainties.

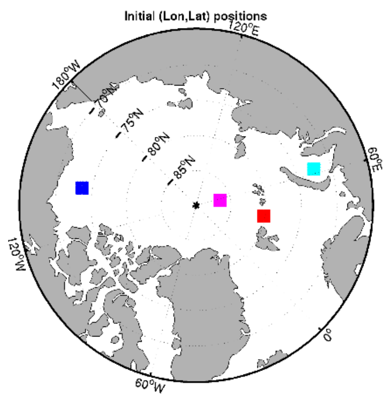

Figure 21: Initial position of the 400 virtual sea ice drifters in the four selected regions of the Arctic, Kara Sea (magenta), Barents Sea (red), Beaufort Sea (blue), and Transpolar drift (cyan).

5.3.4 Results

As examples of ensemble trajectories, we show in figure 22 a sub-sample of the synthetic Lagrangian drifters for all ensemble members. These are commonly referred to as "spaghetti plots" in the probabilistic forecast community. They illustrate different situations:

- Kara Sea: Large displacements and large spread of the end points of ensemble trajectories end points. However, the "spaghettis" look similar in different places, indicating a spatially homogeneous uncertainty.
- Barents Sea: Large displacement and large spread comparable to the Kara Sea, but a stronger dependence on the initial location of the trajectories than in the Kara Sea (inhomogeneous uncertainties). Shorter trajectories tend to have smaller uncertainties associated to them.
- Beaufort Sea: Shorter trajectories, smaller uncertainties and a rather homogeneous uncertainty.
- Transpolar Drift: Long trajectories, but small uncertainties. Both the trajectories and their uncertainties are relatively uniformly distributed in space.

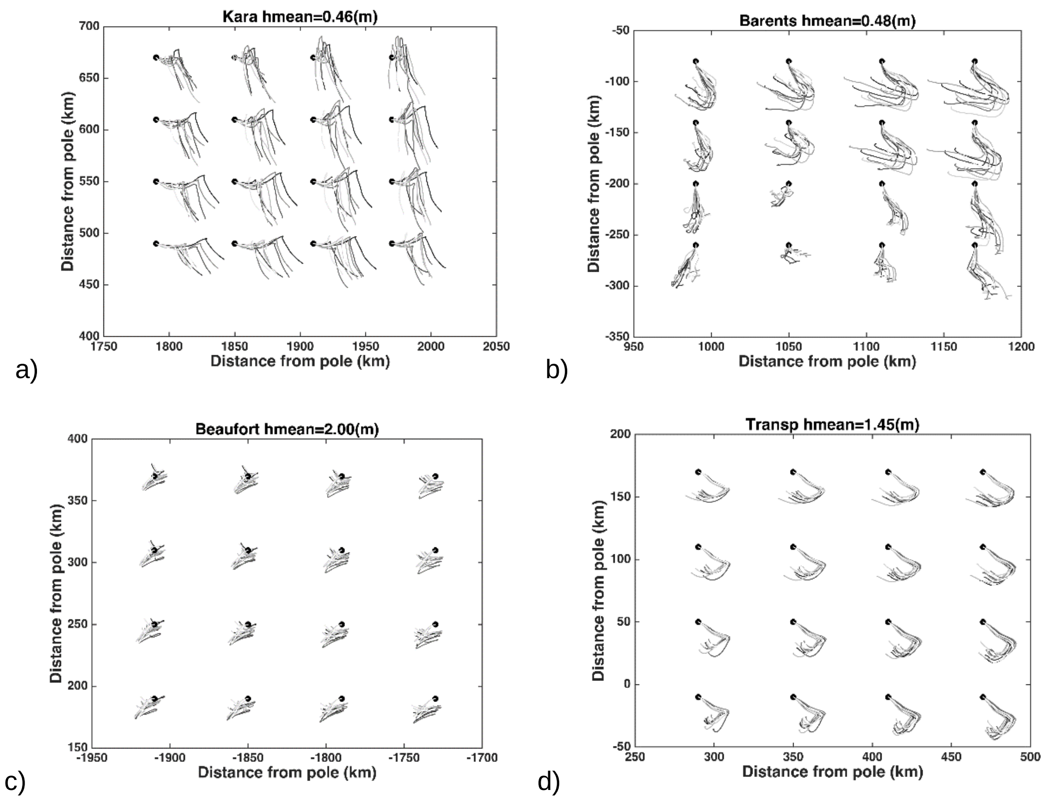

Figure 22: Float tracks in the selected areas a) Kara Sea, b) Barents Sea, c) Beaufort Sea, and d) Transpolar drift with all ten-ensemble members (grey scale). For clarity only every third float track in the initial grid is plotted, 16 out of total 100 floats. The total mean (space, time, ensemble) in each area, of sea ice thickness (hmean) is indicated.

The difference in trajectories due to different forcing can be thought of as the uncertainty in the modelled trajectory due to uncertainty in the applied forcing. We express the trajectory uncertainty of a single trajectory as the standard deviation of the distance between different end points in the ensemble, at time *t* for float number *n*:

$$STD(t,n) = \sqrt{\frac{1}{n}\left(\sum_{i=1}^{N}(X^i - \bar{X})^2 + \sum_{i=1}^{N}(Y^i - \bar{Y})^2\right)} \qquad (7)$$

where N is the ensemble size (N=10), X and Y are the geographical coordinates in polar stereographic projection, corrected for distortion at large distance from the North Pole. We then calculate the mean trajectory uncertainty over all floats (N_f) within each geographical area:

$$\overline{STD}(t) = \frac{1}{N_f}\sum_{n=1}^{N_f} STD(t,n) \qquad (8)$$

For the sake of brevity, we refer to the mean trajectory uncertainty simply as the trajectory uncertainty in this report. The results of these calculations are summarised in table 1.

Area	**Kara**	**Barents**	**Beaufort**	**Transpolar Drift**
Ice Concentration (%)	99	99	99	99
Ice Thickness (m)	0.46	0.48	2.00	1.45
1 day trajectory uncertainty (km)	2.16 +/- 0.10	2.25+/- 0.47	0.93 +/- 0.06	0.96+/- 0.09
3-days trajectory uncertainty (km)	6.55 +/- 0.69	4.53 +/- 1.00	2.11 +/- 0.09	1.57 +/- 0.27
1-week trajectory uncertainty (km)	11.36 +/- 1.16	9.66 +/ -2.53	4.03 +/ -0.38	4.46 +/- 0.41

Table 1: Summary table of ice conditions, trajectory uncertainty at forecast horizons 1 day, 3 days and 7 days, together with their spatial variability within each geographical 200×200 km area.

In figure 23, we show the trajectory uncertainty as a function of the forecast horizon for each area. This shows an increase in the trajectory uncertainty with increasing forecast horizon, except for some fluctuations which we attribute to the weather situation during the 1-week long experiment (for example the bump between days 3 and 4 in the Kara Sea is certainly insignificant). The trajectory uncertainty increases three times faster in thin ice than in thick ice, and since the ratio of ice thickness is also three we can suggest as a rule of thumb an inverse dependency on the ice thickness:

$$\overline{STD}(t) \approx \frac{750\frac{m^2}{d}}{h} t, \qquad (9)$$

where *h* is the ice thickness, measured in meters and *t* is the forecast horizon, measured in days. This relationship is consistent with the linear dependency of the ice “strength” to the ice thickness in the EVP model (Hunke1997). The spatial fluctuations of the ensemble spread are twice as large in the Barents Sea as in the Kara Sea, which is a result of the geographic configuration of these two areas: The Kara Sea is almost completely enclosed by land while the Barents Sea is exposed to the open ocean so the ice cover is more free to diverge there.

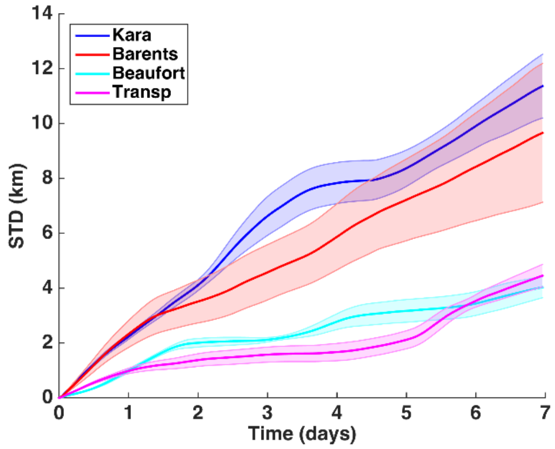

Figure 23: The average trajectory uncertainty, STD (km), due to uncertainties in the wind forcing field in Kara Sea (magenta line), Barents Sea (red line), Beaufort Sea (blue line), and Transpolar drift (cyan line). The transparent colours indicate the standard de deviation of the trajectory uncertainty within each area.

5.3.5 Conclusions

The results in this report indicate that the trajectory uncertainty increases quasi linearly with the forecast horizon but the rate of increase varies geographically by a factor of three between the different regions selected. As a rough guideline, the trajectory uncertainty seems to vary in inverse proportion to the ice thickness. A comparison of predicted uncertainties against actual prediction errors from the literature, gathered from different periods and locations, indicates that, for the ice pack, the uncertainties are likely to be underestimated by this sensitivity study (by a factor of 5 to 8). This points towards shortcomings of the EVP rheology as a possible cause for the underestimation. This should be addressed by the development of alternative sea ice rheological models, such as the EB model. For the ice close to the ice edge, the uncertainty due to the atmospheric forcing is of the same order of magnitude as the errors in sea ice drift estimated in Deliverable 3.2, meaning that most of the error could be explained as coming from the forcing. As a conservative estimate, we suggest a practical trajectory uncertainty in sea ice as half of that is used in the open ocean, more specifically in the Nordic Seas: 5 km (instead of 11 km) for 1 day trajectories, 15 km (instead of 31 km) for 3-days trajectories and 35 km for 7-days trajectories in sea ice.

CHAPTER 6. CONCLUSIONS

This report summarises the work done in the three main work packages of this project. In it we have focused on the most important aspects of the work performed and reported on in the seven reports delivered during the project lifetime. The main results and conclusions to be drawn are stated below, on work package and deliverable basis.

In work package one we focused on the development of two new models, the discrete element model (DE) and the elasto-brittle model (EB). The DE model is a completely new development, even though similar, less sophisticated models do exist. The development of the DE model was covered in deliverable D1.1 (section **Error! Reference source not found.**). This new model allows us to consider ice floes of any size and shape, with realistic configurations selected from aerial or satellite images. The collision of floes is handled without interpenetration, with the friction between floes based on Coulombic friction and a restitution coefficient to describe the loss of kinetic energy during collisions. We tested the model against idealised collision scenarios as well as laboratory results, and used it to study the diffusion and dispersion of ice in the marginal ice zone (MIZ), as discussed below. As far as we know, this model is unique and can already provide realistic simulations of ice floes in a MIZ-type environment. During this project, it has proven useful in furthering our understanding of sea ice dynamics in the MIZ. With further development, we expect it could become a very powerful and useful research tool.

The other model developed in work package one was the EB model. Some work had already been done on this model before the project started and our main aims during the project were to transform the model from a limited experimental platform to a fully functional stand-alone sea ice model. This work was covered in deliverable D1.2 (section **Error! Reference source not found.**). The EB model can now be run on a realistic domain covering the Arctic Ocean, Canadian Arctic Archipelago and the Northern Atlantic at a resolution of ~10 km, forced by atmospheric and oceanic fields from reanalysis products. The model can technically run for an arbitrary long time, but in this project, we focused our tests and validation efforts on winter. We have therefore confirmed the model's good performance in winter, but no such test has been done for the summer months. The main reason for this focus is more availability and better reliability of remote sensing products in winter, as well as the fact that some of the most serious dynamical problems faced by conventional sea ice models are apparent in winter. These are adequately addressed by the EB model as discussed in further detail below. Considering the summer season offers little additional advantage over the winter, with the added difficulty of correctly capturing the melt of the ice. The EB model has proven itself as a very useful tool in this project, producing some of the best and most interesting results of the project. We believe that it will become a very powerful and useful research tool in the future and that it will also proof to be useful in forecasting platforms where the ice state is of particular interest.

Studying sea ice dynamics inherently requires one to deal with non-deterministic dynamics, which was the focus of work package two. At the floe scale, the non-deterministic part of the motion mainly comes from collisions between floes, whereas at larger scales, the fluctuations in the motion result from the response of the ice to oceanic eddies and passing atmospheric perturbations. These fluctuations largely control the uncertainty of the simulated sea ice trajectories and then the reliability of any sea ice forecast. These fluctuations are also the main drivers for sea ice deformation that controls how two particles of ice separate in time, or in other words how sea ice disperses. To better characterise these fluctuations and their representation by sea ice models, we proposed to use the statistical tools and theories developed in the context of molecular and turbulent diffusion and dispersion. These analyses are of particular interest here since they provide reliable estimates of the mean sea ice drift and of the absolute and relative diffusivity coefficients that may be used directly in sea ice trajectory and oil spill modelling.

In deliverable D2.1 (section **Error! Reference source not found.**), we applied the diffusion analysis to the output of the DE model to characterise sea ice diffusion and dispersion in the “collisional” domain, typical of the MIZ. This analysis is robust and its result consistent with observations and theory. In particular, we identify that the diffusion regime in the MIZ is unique and could be seen as a combination of molecular and turbulent diffusion. We estimate the absolute diffusivity at about $K\sim 1\ m^2/s$ and that the dispersion rate depends on the initial separation length as $L(0)^{\beta}$, with $0.17<\beta<0.48$. Our analysis also reveals the high sensitivity to sea ice concentration, especially for the magnitude of the fluctuating velocities.

In deliverable D2.2 (section **Error! Reference source not found.**), we applied the diffusion analysis to the output of the EB and TOPAZ models and to an extensive buoy trajectories dataset, to characterise sea ice diffusion and dispersion in the winter ice pack. Both models and observations indicate a clear transition between the so-called ballistic and Brownian diffusion regimes. However, the TOPAZ model overestimates by far the mean and the fluctuating sea ice velocities. The spatial and statistical distributions of the mean and fluctuating drift simulated by the EB model correspond very well to the ones observed, while those simulated by TOPAZ correspond significantly worse to the observations. Finally, we estimate how the distance between the trajectory predicted by the mean drift and the actual trajectories evolves in time and used this information to provide an estimate of the search areas for sea ice forecasting over time scales larger than a few days. From the buoy dataset, the dispersion rate has been evaluated and found to depend on the initial separation length as $L(0)^{\beta}$ with $\beta\sim 1.8$. This dependence is twice as large as for the ocean surface, leading to a much smaller dispersion rate at small scales (i.e. about 10 km).

Work package three focused on uncertainties due to uncertainties in initial conditions, model parameters, and uncertainties in boundary conditions. In order to address the role of initial conditions we produced a data set of lead and thin ice fraction suitable for initialising the EB model in particular. This work is described in deliverable D3.1 (section **Error! Reference source not found.**). These data were produced from observations from the AMSR2 satellite, giving a continuation of earlier data available from AMSR-E. We then validated the resulting lead fraction data set against manually analyzed SAR data. This comparison showed that the new lead fraction data reproduces well the location and size of larger leads, but leads smaller than ~500 m are usually not recognised by the algorithm. This results in an underestimation of the total lead area by 30-40%. This is a similar result as can be seen in previous studies.

In deliverable D3.2 (section

) we focused on testing and tuning the EB model beyond what we had already done in work package two w.r.t. diffusion and dispersion. We found that the EB model produces sea ice deformation fields showing similar statistical properties to those observed. These statistical properties are closely related to the ice drift itself, as well as the diffusion and dispersion in the pack. In addition, we also quantified how the deformation simulated by the model is sensitive to the model’s mechanical parameters and initial conditions, and used this to define an optimal set of mechanical parameters. We also proposed an innovative method to calibrate the drag parameters and showed how this calibration reduces the median error in the simulated velocity to about 3-5 km per day for sea ice in free drift mode. The calibrated EB model was used in work package two and to produce the data delivered as a part of deliverable D4.2.

In deliverable D3.3 (section

) we estimated the uncertainties in trajectory projections due to uncertainties in forcing, using the TOPAZ model. To do this we used the model perturbation scheme used by the data assimilation system of TOPAZ. This task considers the effects of uncertainties arising from random errors in atmospheric and ocean forcing on the trajectories. It is the first time that such a probabilistic numerical forecast is attempted for sea ice drift. We found that the trajectory uncertainty seems to vary roughly in inverse proportion to the ice thickness. In regions close to the ice edge, the uncertainty due to the forcing may explain most of the error in the simulated sea ice drift. In regions where sea ice is thicker and less fragmented, the errors due to the uncertainties in the forcing are 5-8 times smaller than the actual errors of classical sea ice forecast platforms. This could indicate that there is a large potential for improvements and that implementing better rheologies like EB in sea ice forecast platforms could strongly improve the quality of the predicted sea ice drift.

Substantial progress has been made in this project with respect to the development of dynamical sea ice models. The DE model is an interesting research tool with considerable potential, but at the moment little direct practical value due to the high computational cost. The University J. Fourier/CNRS in Grenoble is currently working on improving the DE model in this respect and NERSC and the University J. Fourier/CNRS are working on a joint project proposal to further develop and integrate the DE and the EB models. In terms of practical use, the EB model is considerably more advanced than the DE model. In this project, we show that the EB model already outperforms TOPAZ in all key dynamical aspects. The main drawback of the current version of the EB model is that it cannot yet be coupled to a full ocean or atmospheric model, resulting in limited feedbacks from these systems on the modelled ice. NERSC is currently exploring avenues of funding to couple the EB model to ocean and/or atmospheric models. In a separate project, we have produced a regional sea ice-forecasting platform based on the EB model, which at its current state is functional, but still has to be rigorously evaluated. We are also working on the integration of a wave in ice model with the EB model.

An important part of the project has also been the investigation of the diffusion and dispersion properties of sea ice. This has shown that the EB model is capable of reproducing well the observed diffusion in the ice pack, and indicated that dispersion is also well reproduced in the model. These characteristics are crucial for oil spill trajectory modelling because they dictate how far and in which manner the oil spreads away from the mean flow of the ice. Knowledge of both the mean flow and the diffusion/dispersion properties can be used to give a probabilistic forecast of the spread of an oil spill.

In this project, we have thus worked on what could become the foundations of a comprehensive oil spill trajectory prediction system. For short-term predictions (about a week), one could use ensemble forecast systems, such as the TOPAZ system to predict the movement of the ice. Here our work has shown that using the EB model would give substantially better results than current ice models. Such prediction models will never be able to accurately predict the ice motion on mid-term time scales, but using the mean flow and diffusion/dispersion properties from past model runs one can create a probabilistic forecast covering up to seasonal time scales. This would provide ice drift information for oil spill models on both short and long time scales. The results of this project show that such a system is feasible, even if some technical challenges remain.

CHAPTER 7. BIBLIOGRAPHY

Amante, C., and B. W. Eakins, ETOPO1 Global Relief Model converted to PanMap layer format, 2009.

Amitrano, D., J. R. Grasso, and D. Hantz, From diffuse to localized damage through elastic interaction, *Geophys. Res. Lett.*, *26*, 2109–2112, 1999.

Batchelor, G. K., Diffusion in a field of homogeneous turbulence, *Mathematical Proceedings of the Cambridge Philosophical Society*, *48*, 345–362, 1952.

Beitsch, A., L. Kaleschke, and S. Kern, Investigating high-resolution AMSR2 sea ice concentrations during the February 2013 fracture event in the Beaufort Sea, *Remote Sensing*, *6*, 3,841–3,856, 2014.

Bentsen, M., G. Evensen, H. Drange, and a. D. Jenkins, Coordinate Transformation on a Sphere Using Conformal Mapping, *Monthly Weather Review*, *127*, 2733–2740, 1999.

Bleck, R., An oceanic general circulation model in pressure coordinates, *Ocean Modelling*, *37*, 55.88, 2002.

Bröhan, D., and L. Kaleschke, A Nine-Year Climatology of Arctic Sea Ice Lead Orientation and Frequency from AMSR-E, *Remote Sensing*, *6*, 1451–1475, 2014.

Bromwich, D. H., A. B. Wilson, L.-S. Bai, G. W. K. Moore, and P. Bauer, A comparison of the regional arctic system reanalysis and the global era-interim reanalysis for the arctic, *Quarterly Journal of the Royal Meteorological Society*, pp. n/a–n/a, 2015.

Byrd Polar Research Center, T. O. S. U., Arctic System Reanalysis (ASR) Project, 2012, accessed 1 Jan 2014.

Cavalieri, D., A microwave technique for mapping thin sea ice, *J. Geophys. Res.*, *99*, 12,561–12,572, 1994.

Chassignet, E. P., H. E. Hurlburt, O. M. Smedstad, G. R. Halliwell, P. J. Hogan, A. J. Wallcraft, and R. Bleck, Ocean prediction with the Hybrid Coordinate Ocean Model (HYCOM), *Ocean Weather Forecasting: An Integrated View of Oceanography*, pp. 413–426, 2006.

Chen, Y., A. Davis, Timothy, W. Hager, William, and S. Rajamanickam, Algorithm 887: CHOLMOD, Supernodal Sparse Cholesky Factorization and Update/Downdate, *ACM Transactions on Mathematical Software*, *35*, 22:1–22–14, 2008.

Coon, M., R. Kwok, G. Levy, M. Pruis, H. Schreyer, and D. Sulsky, Arctic Ice Dynamics Joint Experiment (AIDJEX) assumptions revisited and found inadequate, *J. Geophys. Res.*, *112*, C11S90, 2007.

Cottle, R. W., J.-S. Pang, and R. E. Stone, *The Linear Complementarity Problem*, Academic Press, Boston, MA, 1992.

Counillon, F., and L. Bertino, High-resolution ensemble forecasting for the Gulf of Mexico eddies and fronts, *Ocean dynamics*, *59*, 83–95, 2009.

Dee, D. P., S. M. Uppala, a. J. Simmons, P. Berrisford, P. Poli, S. Kobayashi, U. Andrae, M. a. Balmaseda, G. Balsamo, P. Bauer, P. Bechtold, a. C. M. Beljaars, L. van de Berg, J. Bidlot, N. Bormann, C. Delsol, R. Dragani, M. Fuentes, a. J. Geer, L. Haimberger, S. B. Healy, H. Hersbach, E. V. Hólm, L. Isaksen, P. Kå llberg, M. Köhler, M. Matricardi, a. P. Mcnally, B. M. Monge-Sanz, J. J. Morcrette, B. K. Park, C. Peubey, P. de Rosnay, C. Tavolato, J. N. Thépaut, and F. Vitart, The ERA-Interim reanalysis: Configuration and performance of the data assimilation system, *Quarterly Journal of the Royal Meteorological Society*, *137*, 553–597, 2011.

Dierking, W., and T. Busche, Sea ice monitoring by L-band SAR: An assessment based on literature and comparisons of JERS-1 and ERS-1 imagery, *IEEE Trans. Geosci. Remote Sens.*, *44*, 957–970, 2006.

Drange, H., and K. Simonsen, Formulation of air-sea fluxes in the ESOP2 version of MICOM, Tech Rep. 125, *Tech. rep.*, NERSC, Bergen, Norway, 1996.

Drumwright, W., and D. Shell, An evaluation of methods for modeling contact in multibody simulation, in *IEEE International Conference on Robotics and Automation*, 2011.

Dumont, D., Y. Lô°evesque, A. Bihan-Poudec, and E. Bismuth, Image processing report, CITEPH 64-2012 project, *Tech. rep.*, BGO First, Oceanide, 2013.

Evensen, G., Sequential Data assimilation with a nonlinear quasi-geostrophic model using Monte Carlo Methods to forecast error statistics, *Journal of Geophysical Research: Oceans*, *99*, 10,143–10,162, 1994.

Evensen, G., The Ensemble Kalman Filter: theoretical formulation and practical implementation, *Ocean Dynamics*, *53*, 343–367, 2003.

Fichefet, T., and M. a. M. Maqueda, Sensitivity of a global sea ice model to the treatment of ice thermodynamics and dynamics, *Journal of Geophysical Research*, *102*, 12,609, 1997.

Girard, L., J. Weiss, J. M. Molines, B. Barnier, and S. Bouillon, Evaluation of high-resolution sea ice models on the basis of statistical and scaling properties of Arctic sea ice drift and deformation, *Journal of Geophysical Research*, *114*, C08,015, 2009.

Girard, L., S. Bouillon, and J. Weiss, A new modeling framework for sea-ice mechanics based on elasto-brittle rheology, *Annals of Glaciology*, *52*, 123–132, 2011.

Hamlin, G. J., R. B. Kelley, and J. Tornero, Efficient distance calculation using the spherically-extended polytope (S-tope) model, in *IEEE Proc. Int. Conf. Robotics Automat. 3*, pp. 2,502–2,507, 1992.

Hecht, F., *BAMG: bidimensional anisotropic mesh generator*, 1998.

Herman, A., Molecular-dynamics simulation of clustering processes in sea-ice floes, *Phys. Rev. E*, *84*, 2011.

Hibler, W. D., A viscous sea ice law as a stochastic average of plasticity, *J. Geophys. Res.*, *82*, 3932–3938, 1977.

Hopkins, M. A., On the mesoscale interaction of lead ice and floes, *J. Geophys. Res.*, *101*, 18.315–18.326, 1996.

Hopkins, M. A. a. F. S., Formation of an aggregate scale in Arctic sea ice, *J. Geophys. Res.*, *109*, C01,032, 2004.

Hunke, E., and J. Dukowicz, An elastic-viscous-plastic model for sea ice dynamics, *Journal of Physical Oceanography*, pp. 1849–1867, 1997a.

Hunke, E. C., and J. K. Dukowicz, An elastic-viscous-plastic model for sea ice dynamics, *J. Phys. Ocean.*, *27*, 1849–1867, 1997b.

Kern, S., G. Spreen, L. Kaleschke, S. de la Rosa Hön, and G. Heygster, Polynya Signature Simulation Method polynya area in comparision to AMSR-E 98 ghz sea-ice concentrations in the Ross Sea and off the Adélie Coast, Antarctica, for 2002–5: first results, *Ann. Glaciol.*, *46*, 409–418, 2007.

Kreyscher, M., and G. M. Flato, Results of the Sea Ice Model Intercomparison Project: Evaluation of sea ice rheology schemes for use in simulations Project (SIMIP). Four different sea ice theology schemes, *Journal of Geophysical Research*, *105*, 112,299–11,320, 2000.

Kwok, R., E. C. Hunke, W. Maslowski, D. Menemenlis, and J. Zhang, Variability of sea ice simulations assessed with RGPS kinematics, *J. Geophys. Res.*, *113*, 2008.

Kwok, R., L. T. Perdersen, P. Gudmandsen, and S. S. Pang, Large sea ice outflow into the Nares Strait in 2007, *Geophys. Res. Lett.*, *37*, 2010.

Larour, E., H. Seroussi, M. Morlighem, and E. Rignot, Continental scale, high order, high spatial resolution, ice sheet modeling using the ice sheet system model (issm), *Journal of Geophysical Research: Earth Surface*, *117*, n/a–n/a, 2012, f01022.

Lemieux, J. F., B. Tremblay, J. Sedlacek, P. Tupper, S. Thomas, H. D, and J. P. Auclair, Improving the numerical convergence of viscous-plastic sea ice models with the Jacobian-free Newton-Krylov method, *J. Comp. Phys.*, *229*, 2840–2852, 2010.

Lemieux, J.-F., B. L. Tremblay, F. Dupont, M. Plante, G. C. Smith, and D. Dumont, A basal stress parameterization for modeling landfast ice, *Journal of Geophysical Research: Oceans*, *120*, 3157–3173, 2015.

Marsan, D., and J. Weiss, Space/time coupling in brittle deformation at geophysical scales, *Earth Planet. Sci. Lett.*, *296*, 353–359, 2010.

Marsan, D., H. L. Stern, R. Lindsay, and J. Weiss, Scale dependence and localization of the deformation of Arctic sea ice, *Phys. Rev. Lett.*, *93*, 178,501, 2004.

Marsan, D., J. Weiss, J.-P. Metaxian, J. Grangeon, P.-F. Roux, and J. Haapala, Low-frequency bursts of horizontally polarized waves in the Arctic sea-ice cover, *J. Glaciol.*, *57*, 231–237, 2011.

Martin, S., and A. S. Thorndike, Dispersion of sea ice in the bering sea, *Journal of Geophysical Research: Oceans*, *90*, 7223–7226, 1985.

Massonnet, F., H. Goosse, T. Fichefet, and F. Counillon, Calibration of sea ice dynamic parameters in an ocean-sea ice model using an ensemble Kalman filter, *Journal of Geophysical Research: Oceans*, *119*, 4168–4184, 2014.

McNamara, S., *Discrete Numerical Modeling of Granular Materials*, chap. Event-driven Method, Wiley-ISTE, 2011.

Melsom, A., F. Counillon, J. LaCasce, and L. Bertino, Forecasting search areas using ensemble ocean circulation modeling, *Ocean Dynamics*, *62*, 1–13, 2012.

Miller, P. A., S. W. Laxon, and D. L. Feltham, Optimization of a sea ice model using basinwide observations of Arctic sea ice thickness, extent, and velocity, *J. Climate*, *19*, 1089–1108, 2006.

Quinlan, S., Efficient distance computation between non-convex objects, in *Proceedings International Conference on Robotics and Automation*, pp. 3,324–3,329, 1994.

Rampal, P., J. Weiss, D. Marsan, R. Lindsay, and H. Stern, Scaling properties of sea ice deformation from buoy dispersion analysis, *Journal of Geophysical Research: Oceans*, *113*, n/a–n/a, 2008, c03002.

Rampal, P., J. Weiss, and D. Marsan, Positive trend in the mean speed and deformation rate of arctic sea ice, 1979-2007, *Journal of Geophysical Research: Oceans*, *114*, n/a–n/a, 2009a, c05013.

Rampal, P., J. Weiss, D. Marsan, and M. Bourgoin, Arctic sea ice velocity field: General circulation and turbulent-like fluctuations, *Journal of Geophysical Research: Oceans*, *114*, C10,014, 2009b.

Rathod, H. T., K. V. Nagaraja, B. Venkatesudu, and N. L. Ramesh, Gauss Legendre quadrature over a triangle, *Journal of the Indian Institute of Science*, pp. 183–188, 2004.

Richter-Menge, J. A., S. L. McNutt, J. E. Overland, and R. Kwok, Relating Arctic pack ice stress and deformation under winter conditions, *J. Geophys. Res.*, *107*, 8040, 2002.

Röhrs, J., and L. Kaleschke, An algorithm to detect sea ice leads by using AMSR-E passive microwave imagery, *The Cryosphere*, *6*, 343–352, 2012.

Sakov, P., F. Counillon, L. Bertino, K. A. Lisæter, P. R. Oke, and A. Korablev, TOPAZ4: an ocean-sea ice data assimilation system for the North Atlantic and Arctic, *Ocean Science*, *8*, 633–656, 2012a.

Sakov, P., F. Counillon, L. Bertino, K. A. Lisæter, P. Oke, and A. Korablev, TOPAZ4: An ocean sea ice data assimilation system for the North Atlantic and Arctic, *Ocean Sci.*, *8*, 633–662, 2012b.

Schulson, E. M., Compressive shear faults within Arctic sea ice: Fracture on scales large and small, *J. Geophys. Res.*, *109*, 2004.

Shen, H., W. Hibler, and M. Leppäranta, On applying granular flow theory to a deforming broken ice field, *Acta Mechanica*, *63*, 143–160, 1986.

Shen, H. H., M. Leppäranta, and W. D. Hibler III, The role of floe collisions in sea ice rheology, *J. Geophys. Res.*, *92*, 7085–7096, 1987.

Spreen, G., L. Kaleschke, and G. Heygster, Sea ice remote sensing using amsr-e 89-ghz channels, *Journal of Geophysical Research: Oceans*, *113*, n/a–n/a, 2008, c02S03.

Taylor, G. I., Diffusion by Continuous Movements, *Proceedings of The London Mathematical Society*, *s2-20*, 196–212, 1921.

Thorndike, A. S., Diffusion of sea ice, *J. Geophys. Res.*, *91*, 7691–7696, 1986.

Weiss, J., H. L. Stern, and E. M. Schulson, Sea ice rheology from in-situ, satellite and laboratory observations: Fracture and friction, *Earth Planet. Sci. Lett.*, *255*, 1–8, 2007.

Wilchinsky, A. V., D. L. Feltham, and M. A. Hopkins, Effect of shear rupture on aggregate scale formation in sea ice, *J. Geophys. Res.*, *115*, 1–13, 2010.

CHAPTER 8. PUBLICATIONS RELATED TO THE PROJECT

The following publications have been prepared in relation to the project work:

- Bouillon, S. and P. Rampal, Presentation of the dynamical core of neXtSIM, a new sea ice model, *Ocean Modelling*, 91, 23–37, doi:10.1016/j.ocemod.2015.04.005, 2015.
- Rabatel, M., S. Labbé, and J. Weiss, Dynamics of an assembly of rigid ice floes, *Journal of Geophysical Research Oceans*, 120, 5887–5909, doi:10.1002/2015JC010909, 2015.
- Rampal, P., S. Bouillon, E. Olason, and M. Morlighem, neXtSIM: a new Lagrangian sea ice model, *The Cryosphere Discussions*, 9, 5885–5941, doi:10.5194/tcd-9-5885-2015, 2015.